

NASA CONTRACTOR
REPORT

NASA CR-179135

A FINITE ELEMENT COMPUTATIONAL METHOD FOR HIGH
REYNOLDS NUMBER LAMINAR FLOWS

By Sang-Wook Kim
Universities Space Research Association
Systems Dynamics Laboratory
Science and Engineering Directorate

Interim Report

July 1987

Prepared for
NASA-Marshall Space Flight Center
Marshall Space Flight Center, Alabama

(NASA-CR-179135) A FINITE ELEMENT
COMPUTATIONAL METHOD FOR HIGH REYNOLDS
NUMBER LAMINAR FLOWS Interim Report
(Universities Space Research Association)
48 p Avail: NTIS HC A03/MF A01 CSCL 20D G3/34

N87-27153

Unclas
0092588

1. REPORT NO. NASA CR - 179135		2. GOVERNMENT ACCESSION NO.		3. RECIPIENT'S CATALOG NO.	
4. TITLE AND SUBTITLE A Finite Element Computational Method for High Reynolds Number Laminar Flows				5. REPORT DATE July 1987	
				6. PERFORMING ORGANIZATION CODE	
7. AUTHOR(S) Sang-Wook Kim *				8. PERFORMING ORGANIZATION REPORT #	
9. PERFORMING ORGANIZATION NAME AND ADDRESS George C. Marshall Space Flight Center Marshall Space Flight Center, Alabama 35812				10. WORK UNIT NO.	
				11. CONTRACT OR GRANT NO. NAS8-35918	
12. SPONSORING AGENCY NAME AND ADDRESS National Aeronautics and Space Administration Washington, D.C. 20546				13. TYPE OF REPORT & PERIOD COVERED Contractor Report	
				14. SPONSORING AGENCY CODE	
15. SUPPLEMENTARY NOTES *Universities Space Research Association Prepared by Earth Science and Applications Division, Systems Dynamics Laboratory, Science and Engineering Directorate.					
16. ABSTRACT A velocity-pressure integrated, mixed interpolation, Galerkin finite element method for the Navier-Stokes equations is presented. In the method, the velocity variables are interpolated using complete quadratic shape functions, and the pressure is interpolated using linear shape functions which are defined on a triangular element for the two-dimensional case and on a tetrahedral element for the three-dimensional case. The triangular element and the tetrahedral element are contained inside the complete bi-quadratic and tri-quadratic elements for velocity variables for two- and three-dimensional cases, respectively, so that the pressure is discontinuous across the element boundaries. Example problems considered include: a cavity flow of Reynolds numbers 400 through 10,000; a laminar backward-facing step flow; and a laminar flow in a square duct of strong curvature. The computational results compared favorably with the finite difference computational results and/or experimental data available. It was found that the present method can capture the delicate pressure driven recirculation zones, that the method did not yield any spurious pressure modes, and that the method requires fewer grid points than the finite difference methods to obtain comparable computational results.					
17. KEY WORDS Finite Element Method Navier-Stokes Equations Velocity-pressure Integrated Method			18. DISTRIBUTION STATEMENT Unclassified - Unlimited		
19. SECURITY CLASSIF. (of this report) Unclassified		20. SECURITY CLASSIF. (of this page) Unclassified		21. NO. OF PAGES 47	
				22. PRICE NTIS	

ACKNOWLEDGMENTS

The author would like to express his thanks to Dr. C.-P. Chen for bringing the attention of the author to many valuable references for this work. The author also expresses his thanks to Dr. N. C. Costes for NASA contract NAS8-35918, SSME.

TABLE OF CONTENTS

	Page
I. INTRODUCTION	1
II. FINITE ELEMENT EQUATIONS	2
2-1 The Navier-Stokes Equations	2
2-2 Method of Weighted Residuals and the Galerkin Finite Element Method.....	3
2-3 A New Mixed Interpolation for Velocity and Pressure.....	8
III. EXAMPLE PROBLEMS	10
3-1 A Lid Driven Cavity Flow	10
3-2 A Backward-Facing Step Flow	12
3-3 A Laminar Flow in a Square Duct of Strong Curvature.....	13
IV. CONCLUSIONS AND DISCUSSION	13
REFERENCES	15

LIST OF ILLUSTRATIONS

Figure	Title	Page
1.	Flow elements	20
2.	Configuration, coordinates, and nomenclature of cavity flow.....	21
3.	Discretization of cavity flow	22
4.	Velocity vectors for cavity flow.....	23
5.	Streamlines for cavity flow	25
6.	Pressure contours for cavity flow	27
7.	Horizontal velocity profiles of cavity flow	29
8.	Configuration, coordinates and nomenclature of backward-facing step flow.....	31
9.	Discretization of the backward-facing step flow	32
10.	Velocity vectors for backward-facing step flow.....	33
11.	Streamlines for the backward-facing step flow	34
12.	Pressure contours for the backward-facing step flow.....	35
13.	Reattachment length versus Reynolds number	36
14.	Wall pressure for backward-facing step flow	37
15.	Configuration of the laminar flow in a square duct of strong curvature	38
16.	Discretization of the flow domain	39
17.	Velocity vectors on the curved section.....	40
18.	Secondary recirculation flows	41

LIST OF TABLES

Table	Title	Page
1.	Streamline Contour Label for Cavity Flow	17
2.	Pressure Contour Label for Cavity Flow	17
3.	Stream Function Values at the Center of Vortices for Cavity Flow	18
4.	Streamline Contour Label for Backward-Facing Step Flow.....	19
5.	Pressure Contour Label for Backward-Facing Step Flow	19

CONTRACTOR REPORT

A FINITE ELEMENT COMPUTATIONAL METHOD FOR HIGH REYNOLDS NUMBER LAMINAR FLOWS

I. INTRODUCTION

The finite element computational methods for the Navier-Stokes equations using the primitive variables of velocity and pressure can, in general, be categorized into three groups. These are the velocity-pressure integrated mixed interpolation methods, the penalty methods, and the segregated velocity-pressure solution methods.

In the velocity-pressure integrated mixed interpolation methods, the order of interpolating polynomial for velocity is chosen to be one order higher than that of pressure. For example, if constant elements are used for pressure, then linear elements are used for velocity; and if linear elements are used for pressure, then quadratic elements are used for velocity. Unfortunately, most of the existing velocity-pressure integrated, mixed interpolation methods exhibit spurious pressure modes which become more severe as the Reynolds number is increased, and convergent solution can not be obtained for high Reynolds number flows. Details of the method can be found in Taylor and Hughes [1] and the references therein.

In the penalty method, the pressure variable is pre-eliminated from the Navier-Stokes equations by penalizing the conservation of mass equation, and hence the continuity condition is satisfied approximately. If necessary, pressure can be recovered using the penalized conservation of mass equation in the post process. Unfortunately, most of the computational results obtained using the penalty methods revealed that the conservation of mass equation is not satisfied rigorously so that the computational results deteriorate as the Reynolds number is increased. Details of various penalty methods and the computational results can be found in Zienkiewicz et al. [2], Engelman et al. [3], Kikuchi et al. [4], and Heinrich and Marshall [5], among many others.

Due to the shortcomings of the previous two classes of methods, and partly influenced by the success of the finite difference computational methods of segregated formulation of the Navier-Stokes equations, such as the SIMPLE (Semi-Implicit Method for Pressure-Linked Equations) algorithm [6], the finite element versions of segregated formulation of the Navier-Stokes equations began to appear in recent years [7,8,9]. But the computational results thus obtained did not show any significant improvement over the previous two classes of methods.

The finite element method has certain advantages over the finite difference methods. These advantages are: capability to model complicated domain more precisely, capability to include various boundary conditions more naturally, and capability to show the convergence nature of the method mathematically. For low Reynolds number flows, a number of example cases can be found for which the finite element methods yielded more accurate results than the finite difference methods [10]. But for high Reynolds number flows, the finite difference methods yielded more accurate results, i.e., the finite difference computational results compared more favorably with experimental data than those of the finite element methods, especially when pressure driven recirculation zones exist in the flow field. Thus, the advantages of the finite element method have not been well demonstrated for high Reynolds number viscous flows as yet.

In this report, a new velocity-pressure integrated, mixed interpolation Galerkin finite element method for the Navier-Stokes equations is presented. The finite element system of equations is obtained using the Galerkin finite element method, and the system of equations was solved using a frontal solver [1,11]. The present method yielded accurate computational results for low Reynolds number flows as well as high Reynolds number flows. It was also found that the method can capture subtle pressure driven recirculation zones, and that the method did not yield spurious pressure modes.

II. FINITE ELEMENT EQUATIONS

A finite element computational method for two- and three-dimensional laminar, steady, incompressible flows is described below. The method is based on the integrated velocity-pressure formulation of the Navier-Stokes equations using a new mixed interpolation of velocity and pressure.

In the following discussions, consistent notations are used throughout, and repeated indices imply summation over the indices, unless otherwise specified.

2-1. The Navier-Stokes Equations

The form of the Navier-Stokes equations used herein are given as:

$$\rho u_j \frac{\partial u_i}{\partial x_j} - \frac{\partial \tau_{ij}}{\partial x_j} = b_i \quad \left. \vphantom{\frac{\partial u_i}{\partial x_j}} \right\} \quad \text{in } \Omega \quad (1)$$

$$\frac{\partial u_j}{\partial x_j} = 0 \quad (2)$$

where

$$\tau_{ij} = 2 \mu \epsilon_{ij} - p \delta_{ij} \quad , \quad (3)$$

$$\epsilon_{ij} = \frac{1}{2} \left(\frac{\partial u_i}{\partial x_j} + \frac{\partial u_j}{\partial x_i} \right) \quad , \quad (4)$$

Ω is the open bounded domain of the problem, the subscripts i and j denote coordinate directions, ρ is the density of the fluid, u_i is the velocity component in the i -th coordinate direction, p is the pressure, μ is the molecular viscosity of the fluid, b_i is the body force in the i -th coordinate direction, τ_{ij} is the stress tensor, ϵ_{ij} is the

strain rate tensor, and δ_{ij} is the Kronecker delta such that $\delta_{ij} = 1$ for $i = j$ and $\delta_{ij} = 0$ for $i \neq j$. The boundary conditions used are given as:

$$\underline{u} = \underline{u}_0(\underline{x}) \quad \text{for } \underline{x} \in \partial \Omega_1 \quad (5)$$

$$\underline{T}_i = \tau_{ij} n_j \quad \text{for } \underline{x} \in \partial \Omega_2 \quad (6)$$

$$\partial \Omega_1 \cup \partial \Omega_2 = \partial \Omega \quad (7)$$

$$\partial \Omega_1 \cap \partial \Omega_2 = \phi$$

where $\underline{x} = (x, y)$ for 2-D case and $\underline{x} = (x, y, z)$ for 3-D case, $\partial \Omega$ is the boundary of the domain, $\partial \Omega_1$ is part of the boundary on which Dirichlet boundary condition is specified, $\partial \Omega_2$ is another part of the boundary on which Neumann boundary condition is specified, \underline{T}_i is the surface traction, and ϕ is the null space. A Dirichlet pressure boundary condition is specified at an arbitrary pressure node in the flow domain.

2-2. Method of Weighted Residuals and the Galerkin Finite Element Method

In the context of the method of weighted residuals, the test function for the momentum equation and the conservation of mass equation are denoted as $W_u(\underline{x})$ and $W_p(\underline{x})$, respectively. The weak form of the Navier-Stokes equations are obtained to be:

$$\int_{\Omega} W_u \left(\rho u_j \frac{\partial u_i}{\partial x_j} - \frac{\partial \tau_{ij}}{\partial x_j} - b_i \right) d\underline{x} = 0 \quad (8)$$

$$\int_{\Omega} W_p \left(\frac{\partial u_j}{\partial x_j} \right) d\underline{x} = 0 \quad (9)$$

Integrating by parts of the term containing the stress tensor in equation (8) yields:

$$\int_{\Omega} \left\{ W_u \rho u_j \frac{\partial u_i}{\partial x_j} + \frac{\partial W_u}{\partial x_j} \tau_{ij} - W_u b_i \right\} d\underline{x} - \int_{\partial \Omega_2} W_u \tau_{ij} n_j ds = 0 \quad (10)$$

where $\int_{\partial \Omega_1} W_u \tau_{ij} n_j ds$ term has been dropped out since the test function $W_u(\underline{x})$ vanishes on the boundary $\partial \Omega_1$.

In order to apply the finite element method to the weak form of the Navier-Stokes equations, equations (9) and (10), the global domain is discretized into a number of closed bounded subregions, called the finite elements (Ω_e), such that

$$\begin{aligned}\bar{\Omega}_e &= \Omega_e \cup \partial \Omega_e \\ \bar{\Omega}_h &= \bigcup_{e=1}^E \bar{\Omega}_e \\ \bar{\Omega} &\approx \bar{\Omega}_h\end{aligned}\tag{11}$$

$$\Omega_e \cap \Omega_f = \phi \quad \text{if } i \neq j$$

where each $\bar{\Omega}_e$ is the closure of Ω_e , $\partial \Omega_e$ is the boundary of Ω_e , $\bar{\Omega}_h$ is the finite element approximation of the closed bounded domain $\bar{\Omega}$, and E is the total number of elements.

Introducing the finite element discretization into equations (9) and (10) yields:

$$\sum_{e=1}^E \int_{\Omega_e} \left[W_u \left(\rho u_j \frac{\partial u_i}{\partial x_j} \right) + \tau_{ij} \frac{\partial W_u}{\partial x_j} - W_u b_i \right] d\underline{x} - \sum_{e=1}^E \int_{\partial \Omega_{e2}} W_u \tau_{ij} n_j ds = 0 \tag{12}$$

$$\sum_{e=1}^E \int_{\Omega_e} \left[W_p \frac{\partial u_j}{\partial x_j} \right] d\underline{x} = 0 \tag{13}$$

where $\partial \Omega_{e2}$ is the boundary of an element (Ω_e) which lies on the part of the boundary ($\partial \Omega_2$) on which the flux boundary condition is specified.

The flux through inter-element boundaries should be continuous and the normal vectors at the interface of the two adjacent elements are in the opposite directions. Therefore all the inter-element fluxes in equation (12) cancel each other, and only the prescribed flux on the boundary $\partial \Omega_2$ contributes to the final system of equations.

The consequence of eliminating the fluxes across inter-element boundaries in the finite element method is equivalent to enforcing the flux continuity condition across the inter-element boundaries.

Inserting equations (3), (4), and (6) into equation (12) yields:

$$\sum_{e=1}^E \int_{\Omega_e} \left[W_u \rho u_j \frac{\partial u_i}{\partial x_j} + \frac{\partial W_u}{\partial x_j} \mu \left(\frac{\partial u_i}{\partial x_j} + \frac{\partial u_j}{\partial x_i} \right) - \frac{\partial W_u}{\partial x_j} p \delta_{ij} - W_u b_i \right] dx \approx$$

$$- \sum_{e=1}^E \int_{\partial \Omega_{e2}} W_u T_i ds = 0 \quad . \quad (14)$$

The global finite element system of equations are obtained by assembling the element system of equations. Therefore, the discrete finite element system of equations are derived for an arbitrary element in the following discussions.

Let ϕ_m and ψ_n be sets of basis polynomials to interpolate velocities and pressure respectively, i.e.,

$$\left. \begin{aligned} u_i &= u_{im} \phi_m, \quad \text{sum on } m, m = 1, M \\ p &= p_n \psi_n, \quad \text{sum on } n, n = 1, N \end{aligned} \right\} \quad (15)$$

where u_{im} denotes the m -th nodal value of the velocity component u_i , p_n denotes the n -th nodal value of pressure, and M and N are the number of velocity nodes and the number of pressure nodes in an element, respectively.

In the Galerkin finite element method, the test functions are selected from the same space of interpolating polynomials as the trial functions. Then W_u and W_p can be expanded as:

$$\left. \begin{aligned} W_u &= a_k \phi_k, \quad \text{sum on } k, k = 1, M \\ W_p &= b_\ell \psi_\ell, \quad \text{sum on } \ell, \ell = 1, N \end{aligned} \right\} \quad (16)$$

where a_k and b_ℓ should vanish if the corresponding node lies on the part of the boundary on which the Dirichlet boundary condition is specified, respectively; otherwise, a_k and b_ℓ are arbitrary constants.

The finite element system of equations for an element is obtained by substituting equations (15) and (16) into equations (14) and (15), and is given as

$$\int_{\Omega_e} \left[\phi_k \rho u_{jq} \phi_q \frac{\partial \phi_{im}}{\partial x_j} u_{im} + \frac{\partial \phi_k}{\partial x_j} \mu \left(\frac{\partial \phi_m}{\partial x_j} u_{im} + \frac{\partial \phi_q}{\partial x_i} u_{jq} \right) - \frac{\partial \phi_k}{\partial x_j} \psi_n p_n \delta_{ij} - \phi_k b_i \right] dx$$

$$- \int_{\partial \Omega_{e2}} \phi_k T_i ds = 0 \quad (17)$$

$$\int_{\Omega_e} \psi_\ell \frac{\partial \phi_{jq}}{\partial x_j} u_{jq} dx = 0 \quad (18)$$

where the subscript q ranges from 1 to M , and the arbitrariness of the coefficients a_k and b_ℓ have been made use of in deriving equations (17) and (18).

In matrix form, equations (17) and (18) are given as, for the three-dimensional case;

$$\left(\begin{bmatrix} \underline{\underline{C}} & \underline{\underline{0}} & \underline{\underline{0}} \\ (\text{sym}) & \underline{\underline{C}} & \underline{\underline{0}} \\ & & \underline{\underline{C}} \end{bmatrix} + \begin{bmatrix} \underline{\underline{K}}_0 & \underline{\underline{0}} & \underline{\underline{0}} \\ (\text{sym}) & \underline{\underline{K}}_0 & \underline{\underline{0}} \\ & & \underline{\underline{K}}_0 \end{bmatrix} + \begin{bmatrix} \underline{\underline{K}}_{11} & \underline{\underline{K}}_{12} & \underline{\underline{K}}_{13} \\ \underline{\underline{K}}_{21} & \underline{\underline{K}}_{22} & \underline{\underline{K}}_{23} \\ \underline{\underline{K}}_{31} & \underline{\underline{K}}_{32} & \underline{\underline{K}}_{33} \end{bmatrix} \right) \begin{Bmatrix} u_1 \\ u_2 \\ u_3 \end{Bmatrix}$$

$$- \begin{Bmatrix} Q_1 \\ Q_2 \\ Q_3 \end{Bmatrix} \{ p \} = \begin{Bmatrix} f_1 \\ f_2 \\ f_3 \end{Bmatrix} + \{ \text{b.c.} \} \quad (19)$$

$$[Q_1^T \quad Q_2^T \quad Q_3^T] \begin{Bmatrix} u_1 \\ u_2 \\ u_3 \end{Bmatrix} = \{0\} \quad (20)$$

where

$$\underline{\underline{C}} = \int_{\Omega_e} \underline{\underline{\phi}}^T \rho (\underline{u}_j^T \underline{\underline{\phi}}) \frac{\partial \underline{\underline{\phi}}}{\partial x_j} d\mathbf{x} \quad , \quad (21)$$

$$\underline{\underline{K}}_0 = \int_{\Omega_e} \frac{\partial \underline{\underline{\phi}}^T}{\partial x_j} \mu \frac{\partial \underline{\underline{\phi}}}{\partial x_j} d\mathbf{x} \quad , \quad (22)$$

$$\underline{\underline{K}}_{ij} = \int_{\Omega_e} \frac{\partial \underline{\underline{\phi}}^T}{\partial x_j} \mu \frac{\partial \underline{\underline{\phi}}}{\partial x_i} d\mathbf{x} \quad , \quad (23)$$

$$\underline{\underline{Q}}_i = \int_{\Omega_e} \frac{\partial \underline{\underline{\phi}}^T}{\partial x_i} \underline{\underline{\psi}} d\mathbf{x} \quad , \quad (24)$$

$$\underline{f}_i = \int_{\Omega_e} \underline{\underline{\phi}}^T b_i d\mathbf{x} \quad , \quad (25)$$

\underline{u}_i is a column vector of nodal values of the velocity component u_i , \underline{p} is a column vector of nodal pressure, $\underline{\underline{\phi}}$ is a column vector of interpolating polynomials for velocity, $\underline{\underline{\psi}}$ is a column vector of interpolating polynomials for pressure, {b.c.} is a column vector contributed by the specified flux boundary condition, and the subscripts i and j range from one up to the number of spatial dimensions, respectively.

For the two-dimensional case, the element system of equations can be obtained by deleting the appropriate third row and column sub-matrices from equations (19) and (20).

The integrations in equations (21) through (25) were evaluated using the Gauss numerical quadrature method with three Gauss points for each coordinate direction. The assembled global system of equations was solved by a direct (Picard) iteration method using a frontal solver [1,12], and the solutions were updated using an under-relaxation method given as:

$$a_j^* = \alpha a_j^n + (1 - \alpha) a_j^{n-1} \quad (26)$$

where a_j represents any degree of freedom, α is the under-relaxation number, the superscripts n and $n-1$ denote iteration levels, and a_j^* is the updated solution. $\alpha = 1$ (no under-relaxation) was used for all the flow variables for low Reynolds number flows; and $\alpha = 0.8$ for velocities and $\alpha = 1$ for pressure were used for high Reynolds number flows.

2-3. A New Mixed Interpolation for Velocity and Pressure

The new flow elements used in the present finite element computation of Navier-Stokes equations are introduced in this section. For two-dimensional case, the velocities are interpolated using the biquadratic shape functions and the pressure is interpolated using the linear shape functions defined on a triangular element which is contained inside the quadratic element, as shown in Figure 1-a. The three pressure nodes are located at the three Gauss points of the three-point Gauss quadrature rule for quadrilateral elements [13], i.e., the same locations as those used in the Reduced Integration Penalty (RIP) method. The coordinates of the pressure nodes on the computational element are given as:

$$\xi_n = \begin{cases} (0, \sqrt{2}/\sqrt{3}) & \text{for } n = 1 \\ (-1/\sqrt{2}, -1/\sqrt{6}) & \text{for } n = 2 \\ (1/\sqrt{2}, -1/\sqrt{6}) & \text{for } n = 3 \end{cases} \quad (27)$$

where $\xi_n = (\xi_n, \eta_n)$ for 2-D case, and n denotes the pressure node numbers. The shape functions for each of the nodes are given as:

$$\left. \begin{aligned} \psi_1 &= \frac{1}{3} + \frac{\sqrt{2}}{\sqrt{3}} \eta \\ \psi_2 &= \frac{1}{3} - \frac{1}{\sqrt{2}} \xi - \frac{1}{\sqrt{6}} \eta \\ \psi_3 &= \frac{1}{3} + \frac{1}{\sqrt{2}} \xi - \frac{1}{\sqrt{6}} \eta \end{aligned} \right\} \quad (28)$$

For the three-dimensional case, the velocities are interpolated by the tri-quadratic shape functions and the pressure is interpolated using the linear shape functions defined on a tetrahedral element which is contained inside the tri-quadratic brick element, as shown in Figure 1-b. The coordinates of the pressure nodes on the computational element are given as:

$$\xi_n = \begin{cases} (0, \sqrt{2}/\sqrt{3}, -1/\sqrt{3}) & \text{for } n = 1 \\ (0, -\sqrt{2}/\sqrt{3}, -1/\sqrt{3}) & \text{for } n = 2 \\ (\sqrt{2}/\sqrt{3}, 0, 1/\sqrt{3}) & \text{for } n = 3 \\ (-\sqrt{2}/\sqrt{3}, 0, 1/\sqrt{3}) & \text{for } n = 4 \end{cases} \quad (29)$$

where $\xi_n = (\xi_n, \eta_n, \zeta_n)$ for the 3-D case, and n denotes the node numbers of the pressure nodes. The shape functions for each of the pressure nodes are given as:

$$\left. \begin{aligned} \psi_1 &= \frac{1}{4} + \frac{1}{2} \frac{\sqrt{3}}{\sqrt{2}} \eta - \frac{\sqrt{3}}{4} \zeta \\ \psi_2 &= \frac{1}{4} - \frac{1}{2} \frac{\sqrt{3}}{\sqrt{2}} \eta - \frac{\sqrt{3}}{4} \zeta \\ \psi_3 &= \frac{1}{4} + \frac{1}{2} \frac{\sqrt{3}}{\sqrt{2}} \xi + \frac{\sqrt{3}}{4} \zeta \\ \psi_4 &= \frac{1}{4} - \frac{1}{2} \frac{\sqrt{3}}{\sqrt{2}} \xi + \frac{\sqrt{3}}{4} \zeta \end{aligned} \right\} \quad (30)$$

The shape functions given in equations (28) and (30) satisfy the relationship that:

$$\psi_\ell(\xi_n) = \begin{cases} 1 & \text{if } \ell = n \\ 0 & \text{if } \ell \neq n \end{cases} \quad (31)$$

where ψ_ℓ is the shape function for the ℓ -th pressure node and ξ_n denotes the coordinates of the n -th pressure node. Additional pressure interpolation polynomials tested for two-dimensional flows were $\psi^T = (1, x, y)$. The latter interpolation scheme yielded the same computational results, up to several significant digits, as equation (28) for low Reynold number flows. As the Reynolds number is increased, i.e., Reynolds number of 10,000 case for the cavity flow, the pressure interpolation polynomials given in equation (28) were found to be the most stable numerically.

III. EXAMPLE PROBLEMS

The finite element method described in the previous sections was tested and validated by solving a few example problems for which vast amounts of computational results and/or experimental data were available. These are: a lid driven cavity flow [5,14-18], a laminar backward-facing step flow [19-21], and a laminar flow in a square duct of strong curvature [22,23].

In the following discussions, solving the coupled momentum equation and the conservation of mass equation once is counted as an iteration. The convergence criterion used was

$$\left| 1 - \frac{a_j^{n+1}}{a_j^n} \right| < \epsilon, \quad j = 1, T \quad (32)$$

where a_j denotes a nodal value of velocity component or pressure; T is the number of total degrees of freedom; and ϵ is the convergence criterion. $\epsilon = 1 \times 10^{-4}$ was used for the two-dimensional flow cases; and $\epsilon = 1 \times 10^{-3}$ for the three-dimensional flow case. In elliptic flow computations, the velocity component may become vanishingly small near the stagnation regions, separation regions, and reattachment regions. Also pressure may become vanishingly small in some regions of the flow field. For these cases, i.e., $a_j^n \approx 0$, it can be expected that equation (32) can hardly be satisfied. Therefore, equation (32) needs to be further supplemented by other constraint(s). For the present case, any velocity degree of freedom (a_j^n) whose relative magnitude with respect to the maximum velocity in the flow domain is smaller than ϵ_1 , i.e., $|a_j^n/v_{\max}| < \epsilon_1$ and $\epsilon_1 = 1 \times 10^{-4}$, was screened out before equation (32) was applied. By the same way, any pressure degree of freedom (a_j^n) whose relative magnitude with respect to the maximum pressure in the flow domain is less than ϵ_1 , i.e., $a_j^n/p_{\max} < \epsilon_1$, was screened out from the convergence test.

In the new mixed interpolation method introduced herein, the pressure is discontinuous across element boundaries. Thus the nodal pressure at the velocity node was obtained by averaging all the pressure contributions made by the elements containing the node; and each of the contributions was computed using equation (28) for the two-dimensional case and equation (30) for the three-dimensional case.

3-1. A Lid Driven Cavity Flow

The cavity flow is described in Figure 2. No slip boundary condition, i.e., $u = v = 0$, was applied at all the boundaries except at $y = 1$ where $u = 1$ and $v = 0$. The Reynolds numbers considered were 400, 1000, 3200, 5000, 7500, and 10,000; where the Reynolds number is defined as $Re = \rho UL/\mu$, $U = 1$ is the velocity of the lid, and $L = 1$ is the reference length. The Reynolds number was varied by adjusting the viscosity (μ) of the fluid with the remainder of the parameters kept as constants. Two different grids, as shown in Figure 3, were used.

For the coarse grid case (Grid A), convergent solutions were obtained up to a Reynolds number of 3200. But the coarse grid could not resolve the smallest eddies (vortices 4 and 5 in Fig. 2), and thus the grid was not tested for $Re > 3200$. Velocity vectors obtained by using the coarse grid for $Re \leq 1000$ are shown in Figures 4-1 and 4-b, respectively. The streamline contours for $Re \leq 1000$ obtained by using the coarse grid were qualitatively the same as those obtained by using the fine grid (Grid B), but the magnitude of the minimum stream function values at the center of the primary vortex were a few percent smaller than those obtained by using the fine grid.

The velocity vectors ($Re \geq 3200$) and the streamline contours obtained by using the fine grid are shown in Figures 4 and 5, respectively. The streamline contour labels are given in Table 1. In Figure 5, it can be seen that the sizes of vortices 4 and 5 of the present computational results are smaller than those of Schreiber and Keller [15] and Ghia et al. [16]. Details of the smallest eddies (vortices 4 and 5) need to be further studied using finer grid.

The normalized pressure contours for all the Reynolds number cases obtained by using the fine grid are shown in Figure 6, and the pressure contour labels are given in Table 2. The normalized pressure (P) was obtained from the computed static pressure (p) using a relationship that $P = pL_{ref}/V_{ref}\mu$, where $L_{ref} = 1$ is the reference length, $V_{ref} = 1$ is the reference velocity, and μ is the molecular viscosity of the fluid.

The horizontal velocity profiles at $x = 0.5$ are compared with various computational results in Figure 7. For $Re = 400$, it can be seen that the minimum horizontal velocity due to Burggraf [14] is approximately 12 percent smaller than that of Ghia et al. [16], and that the same velocity due to Bercovier and Engelman [18] is approximately 25 percent smaller than the same data. For $Re = 1000$, the horizontal velocity profile due to Bercovier and Engelman [16] further deviates from that of Ghia et al. or the present computational result. In general, the present computational results compare more favorably with those of Ghia et al. than those of Burggraf [14] and Bercovier and Engelman [16], as shown in Figure 7.

For $Re = 10,000$, it can be seen that the horizontal velocity profile due to Schreiber and Keller [15] is slightly different from that of Ghia et al. [16], which shows that the global computational results can be slightly different depending on the order of difference approximation used for the boundary condition. The present computational results compare more favorably with those of Ghia et al. [16] than those of Schreiber and Keller [15]. But both of these finite difference solutions appeared only recently, and it is not quite clear which of these is better as yet.

The local maximum or minimum values of the stream function at the center of vortices for the primary and the first three secondary vortices are compared with those of References 15, 16, and 17 in Table 3. It can be seen that the present computational results, obtained by using approximately one-fourth of the number of grid points used by others, compare favorably with the three data in general.

Computation of the cavity flow was carried out in the order of increasing the Reynolds number. Uniform zero values for both velocity and pressure were used as an initial guess for $Re = 10$, the converged solution for $Re = 10$ was used as an initial guess for $Re = 400$, and so on. The required number of iterations were 5, 15, 25, 42, 51, 60, and 194, for Reynolds numbers of 10, 400, 1000, 3200, 5000, 7500, and 10,000, respectively. The excessive number of iterations required for the $Re = 10,000$ case, using the converged solution of $Re = 7500$ as initial guess, may be due

to the grid which is still not fine enough for the Reynolds number considered. The similar phenomenon was observed when the coarse grid (Grid A) was used to solve the Reynolds number of 3200 case.

Study on the efficiency of the present numerical method has not been made as yet. But based on the required number of grid points and the required number of iterations to achieve comparable accuracy with those of the velocity-pressure based finite difference flow solvers, the present method would not be unduly expensive compared with the finite difference methods.

3-2. A Backward-Facing Step Flow

A laminar backward-facing step flow is considered in the following. A description of the problem is shown in Figure 8, and the experimental data for the flow can be found in Armaly et al. [19]. The Reynolds number, $Re = \rho V D / \mu$, is based on the hydraulic diameter ($D = 0.0104$ meters) and the bulk velocity ($V = 0.6667$ meters/sec) at the inlet. The Reynolds numbers were varied by adjusting the molecular viscosity (μ) of the fluid. For the Reynolds number less than approximately 450, there exists only one recirculation zone at the down-stream region of the backward-facing step. As the Reynolds number is increased beyond approximately 450, another recirculation zone appears at the top wall of the channel, the size of which grows further as the Reynolds number is increased. Experimental data show that a third recirculation zone appears at the bottom wall for the Reynolds number greater than approximately 1000. As the Reynolds number is increased beyond approximately 600, the three-dimensional effect becomes so strong that comparison between the two-dimensional computational result and the experimental data becomes less meaningful, which is discussed in detail in Armaly et al. [19]. Therefore, the computations were carried out from a Reynolds number of 100 up to a Reynolds number of 900 in the order of increasing the Reynolds number by 100 in the present study. For the coarse grid (Grid A) case, the uniform zero values for both velocity and pressure were used as an initial guess for the $Re = 100$ case, the converged solution of the $Re = 100$ case was used as an initial guess for the $Re = 200$ case, and so on. The required number of iterations were 20, 40, 53, 89, 135, 161, 171, 172, and 183 for Reynolds numbers of 100 through 900, respectively. For the fine grid case (Grid B), the initial guess for all the Reynolds number cases were obtained by interpolating the coarse grid solutions using the multi-grid concept of Ghia et al. [16].

The computed velocity vectors and the streamline contours for $Re = 400, 500$, and 800 are shown in Figures 10 and 11. The streamline contour labels are given in Table 4. The onset of the second recirculation zone at the top wall can be seen in the streamline contour plot given in Figure 11-a, yet there exists no recirculation zone for $Re = 400$ as can be confirmed from the velocity vector plot in Figure 10-a.

The computed static pressure was normalized using a relationship $P = p L_{ref} / V_{ref} \mu$, where $L_{ref} = 0.0049$ meters is the step height and V_{ref} is the bulk velocity at the inlet. The normalized pressure contours for Reynolds numbers of 400, 500, and 800 are shown in Figure 12.

The size of recirculation zones versus Reynolds number is compared with experimental data in Figure 13. It can be seen that the computational results compare favorably with experimental data up to Reynolds number of approximately 600.

The top and bottom wall pressure for Reynolds numbers of 100 through 900 are shown in Figure 14. Neither the experimental data nor any other computational result for the wall pressure are available as yet, and no comparison could be made.

Finite difference computation of the same backward-facing step flow can be found in Kim and Moin [20] and Kwak and Chang [21] among many others. The same level of agreement between the computational results and the experimental data as the present case can be found in Kim and Moin [20]. On the other hand, the streamline contour plot due to Kwak and Chang [21] did not show the top wall recirculation zone as clearly as that of the present case or that of Kim and Moin [20].

3-3. A Laminar Flow in a Square Duct of Strong Curvature

A re-developing laminar flow in a square duct of strong curvature is considered below. The flow configuration is shown in Figure 15; and the experimental data for the flow is given in Humphery et al. [22].

The Reynolds number based on the hydraulic diameter of 0.04 m and the bulk velocity of 1.98×10^{-2} m/sec was 790. Due to the symmetry of the flow domain, only one half of the duct was considered in the computation. The inlet plane was located 2.8 hydraulic diameters upstream of the curved section, and the outlet plane was 8 hydraulic diameters downstream. Discretization of the domain is shown in Figure 16. An analytical solution for the fully developed duct flow was prescribed at the inlet plane of the duct, and a vanishing normal stress boundary condition was prescribed at the exit.

The computed velocity vectors at the three planes of the curved section are shown in Figure 17. It can be seen in Figure 17-c that there exists a weak recirculation zone extending up to $\theta = 40^\circ$ of the curved section. Computational results due to Humphery et al. [22] showed that the same recirculation zone extended beyond $\theta = 12^\circ$, and the computational results due to Rhie [23] showed that the recirculation zone extended beyond $\theta = 30^\circ$. There does not exist fine grid computational results for the recirculation zone as yet. The secondary recirculation flows at three cross-sections are shown in Figure 18. The computational results showed that the grid used was not fine enough to resolve all the details of the flow field. It was also found that the frontal solver used in this study was not adequate to pursue further grid refinement. Fine grid computational results for the laminar flow in a square duct of strong curvature and other three-dimensional flow cases will be reported in the near future.

IV. CONCLUSIONS AND DISCUSSION

A new velocity-pressure integrated, mixed interpolation finite element method for the Navier-Stokes equations has been presented. The method has been tested for cavity flows with Reynolds number of 400 up to 10,000, a backward facing-step-flow of Armaly et al. [19], and a laminar flow in a square duct of strong curvature of Humphery et al. [22].

For the cavity flows, the present computational results compared favorably with those of Schreiber and Keller [15], Ghia et al. [16], and Gresho et al. [17], which were obtained by using approximately four times more grids than the present case.

For the backward-facing step flow, it was shown that the present computational method could capture the subtle pressure driven secondary recirculation zone at the top wall of the channel for Reynolds numbers greater than 500. The size of the recirculation zone also compared favorably with the experimental data.

For the three-dimensional curved duct flow, grid refinement was not feasible due to the computer limitation and the frontal solver used in the present study. Detailed fine grid computation of the laminar flow in a square duct of strong curvature [22] will be reported in a near future together with other three-dimensional flow cases.

It is usually known that the Bubnov-Galerkin method [24] (i.e., the test functions are selected from the same space as that of the trial functions, as in the present case) yields oscillatory solutions for high Reynolds number flows. An extensive discussion on the finite element upwinding technique can be found in Brooks and Hughes [24] among many others. But the present computational results showed that no upwinding was necessary to obtain accurate solutions which are free of wiggles for the Navier-Stokes equations.

REFERENCES

1. Taylor, C., and Hughes, T. G.: Finite Element Programming of the Navier-Stokes Equation. Pineridge Press, Swansea, U.K., 1980.
2. Zienkiewicz, O. C.; Taylor, R. L.; and Baynham, J. M. W.: Mixed and Irreducible Formulations in Finite Element Analysis. Eds. S. N. Atluri, et al., Hybrid and Mixed Finite Element Methods, J. Wiley and Sons, New York, 1983.
3. Engelman, M. S.; Sani, R. L.; Gresho, P. M.; and Bercovier, M.: Consistent versus Reduced Integration Penalty Methods for Incompressible Media Using Several Old and New Elements. *Int. J. Nume. Meth. Fluids*, Vol. 2, 1982, pp. 25-42.
4. Kikuchi, N.; Oden, J. T.; and Song, Y. J.: Convergence of Modified Penalty Methods and Smoothing Schemes of Pressure for Stokes' Flow Problems. Finite Elements in Fluids, Vol. 5, Eds. R. H. Gallagher, et al., J. Wiley and Sons, New York, 1984, pp. 107-126.
5. Heinrich, J. C., and Marshall, R. S.: Viscous Incompressible Flow by Penalty Function Finite Element Method. *Computers and Fluids*, Vol. 9, 1981, pp. 73-83.
6. Patankar, S. V.: Numerical Heat Transfer and Fluid Flow. McGraw-Hill, New York, 1980.
7. Comini, G., and Giudice, S. D.: Finite Element Solution of the Incompressible Navier-Stokes Equations. *Numerical Heat Transfer*, Vol. 5, 1986, pp. 223-237.
8. Benim, A. C., and Zinser, W.: A Segregated Formulation of Navier-Stokes Equations with Finite Elements. *Comput. Meth. Appl. Mech. Engrg.*, Vol. 57, 1986, pp. 223-237.
9. Rice, J. G., and Schnipke, R. J.: An Equal-Order Velocity-Pressure Formulation That Does Not Exhibit Spurious Pressure Modes. *Comput. Meth. Appl. Mech. Engrg.*, Vol. 58, 1986, pp. 135-149.
10. Eds. R. H. Gallagher, et al.: Finite Elements in Fluids. Vol. 1-6, J. Wiley and Sons, New York.
11. Oden, J. T., and Reddy, J. N.: An Introduction to the Mathematical Theory of Finite Elements, J. Wiley and Sons, New York, 1976.
12. Irons, B., and Ahmad, S.: Techniques of Finite Elements, J. Wiley and Sons, New York, 1980.
13. Dhatt, G., and Touzot, G.: The Finite Element Method Displayed, Translated by G. Cantin., J. Wiley and Sons, New York, 1984.
14. Burggraf, O. R.: Analytical and Numerical Studies of the Structure of Steady Separated Flows. *J. Fluid Mech.*, Vol. 24, 1966, pp. 113-151.
15. Schreiber, R., and Keller, H. B.: Driven Cavity Flows by Efficient Numerical Techniques. *J. Comput. Physics*, Vol. 49, 1983, pp. 310-333.

16. Ghia, U.; Ghia, K. N.; and Shin, C. T.: High-Re Solutions for Incompressible Flow Using the Navier-Stokes Equations and a Multigrid Method. *J. Comput. Physics*, Vol. 48, 1982, pp. 387-411.
17. Gresho, P. M.; Chan, S. T.; Lee, R. L.; and Upson, C. D.: A Modified Finite Element Method for Solving the Time-Dependent Incompressible Navier-Stokes Equations, Part 2. Applications. *Int. J. Nume. Meth. Fluids*, Vol. 4, 1984, pp. 619-640.
18. Bercovier, M., and Engelman, M.: A Finite Element for Numerical Solution of Viscous Incompressible Flows. *J. Comput. Physics*, Vol. 30, 1979, pp. 181-201.
19. Armaly, B. F.; Durst, F.; Pereira, J. C. F.; and Schonung, B.: Experimental and Theoretical Investigation of Backward-Facing Step Flow. *J. Fluid Mech.*, Vol. 127, 1983, pp. 473-496.
20. Kim, J., and Moin, P.: Application of a Fractional-Step Method to Incompressible Navier-Stokes Equations. *J. Comput. Physics*, Vol. 59, 1985, pp. 308-323.
21. Kwak, D., and Chang, J. L. C.: A Three-Dimensional Incompressible Navier-Stokes Flow Solver, Part I. - INS3D Code. CFD Workshop, University of Tennessee Space Institute, Tullahoma, Tennessee, June 1985.
22. Humphrey, J. A. C.; Taylor, A. M. K.; and Whitelaw, J. H.: Laminar Flow in a Square Duct of Strong Curvature. *J. Fluid Mech.*, Vol. 83, 1977, pp. 509-527.
23. Rhie, C. M.: A Three-Dimensional Passage Flow Analysis Method Aimed at Centrifugal Impellers. *Computers and Fluids*, Vol. 13, No. 4, 1985, pp. 443-460.
24. Brooks, A. N., and Hughes, T. J. R.: Streamline Upwind/Petrov-Galerkin Formulations for Convection Dominated Flows with Particular Emphasis on the Incompressible Navier-Stokes Equation. *Comput. Meth. Applied Mech. Engrg*, Vol. 32, 1982, pp. 199-259.

TABLE 1. STREAMLINE CONTOUR LABEL FOR CAVITY FLOW

Label	ψ^*	Label	ψ	Label	ψ
A	-0.11	F	-0.03	K	$2.X10^{-4}$
B	-0.10	G	-0.01	L	$5.X10^{-4}$
C	-0.09	H	$-1.X10^{-10}$	M	$1.X10^{-3}$
D	-0.07	I	$1.X10^{-6}$	N	$2.X10^{-3}$
E	-0.05	J	$5.X10^{-5}$		

* ψ : stream function

TABLE 2. PRESSURE CONTOUR LABEL FOR CAVITY FLOW

Label	Reynolds Number (Re)					
	400	1000	3200	5000	7500	10000
A	-40.	-100.	-310.	-470.	-700.	-900.
B	-30.	-70.	-220.	-370.	-500.	-650.
C	-20.	-50.	-120.	-270.	-300.	-400.
D	-10.	-20.	-70.	-150.	-150.	-200.
E	0.	0.	0.	0.	0.	0.
F	10.	30.	100.	120.	300.	400.
G	30.	80.	200.	280.	1000.	1000.
H	50.	---	400.	900.	---	3000.

TABLE 3. STREAM FUNCTION VALUES AT THE CENTER OF VORTICES FOR CAVITY FLOW

	Re _y	Schreiber* & Keller	Ghia ^o et. al.	Gresho ^x et. al.	present ⁺
Primary Vortex	400	-0.1130	-0.1139	---	-0.1128
	1000	-0.1160	-0.1179	-0.114	-0.1169
	3200	---	-0.1204	-0.118	-0.1181
	5000	---	-0.1190	-0.109	-0.1173
	7500	---	-0.1200	-0.108	-0.1157
	10000	-0.1028	-0.1197	-0.101	-0.1150
Vortex 1	400	6.440x10 ⁻⁴	6.4235x10 ⁻⁴	---	6.1810x10 ⁻⁴
	1000	1.700x10 ⁻³	1.7510x10 ⁻³	1.760x10 ⁻³	1.6594x10 ⁻³
	3200	---	3.1396x10 ⁻³	3.290x10 ⁻³	2.6744x10 ⁻³
	5000	---	3.0836x10 ⁻³	3.870x10 ⁻³	2.7786x10 ⁻³
	7500	---	3.2848x10 ⁻³	4.860x10 ⁻³	2.7396x10 ⁻³
	10000	2.960x10 ⁻³	3.4183x10 ⁻³	5.540x10 ⁻³	2.7528x10 ⁻³
Vortex 2	400	1.450x10 ⁻⁵	1.4195x10 ⁻⁵	---	1.3577x10 ⁻⁵
	1000	2.170x10 ⁻⁴	2.3113x10 ⁻⁴	2.0 x10 ⁻⁴	2.1951x10 ⁻⁴
	3200	---	9.7820x10 ⁻⁴	1.20 x10 ⁻³	1.0465x10 ⁻³
	5000	---	1.3612x10 ⁻³	1.490x10 ⁻³	1.2675x10 ⁻³
	7500	---	1.4671x10 ⁻³	1.750x10 ⁻³	1.3697x10 ⁻³
	10000	---	1.5183x10 ⁻³	1.930x10 ⁻³	1.4055x10 ⁻³
Vortex 3	3200	---	7.2786x10 ⁻⁴	5.860x10 ⁻³	6.4440x10 ⁻⁴
	5000	---	1.4564x10 ⁻³	1.230x10 ⁻³	1.3045x10 ⁻³
	7500	---	2.0462x10 ⁻³	1.840x10 ⁻³	1.8426x10 ⁻³
	10000	---	2.4210x10 ⁻³	2.230x10 ⁻³	2.1817x10 ⁻³

* 141x141 grids for Re = 400 and 1000, and 180x180 grids for Re=10,000.

o 257x257 grids for Re = 400, 5000, 7500, and 10,000, and 129x129 grids for Re = 1000 and 3200.

x 129x129 grids for Re<3200 and 257x257 grids for Re>5000.

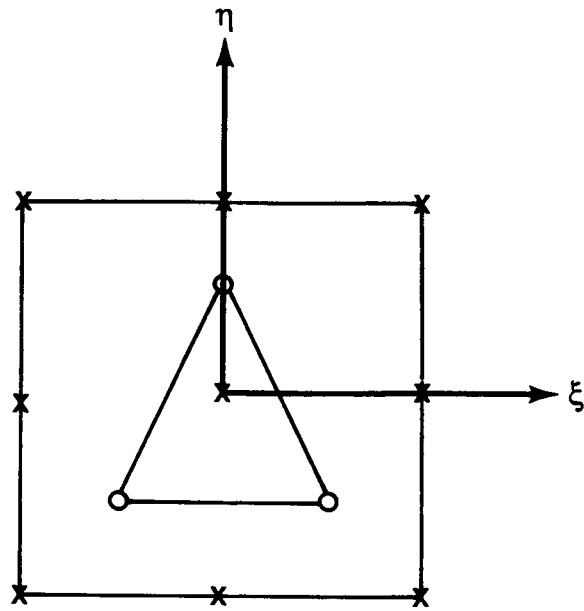
+ 65x65 grids (32x32 quadratic elements) for all the cases.

**TABLE 4. STREAMLINE CONTOUR LABEL FOR
BACKWARD-FACING STEP FLOW**

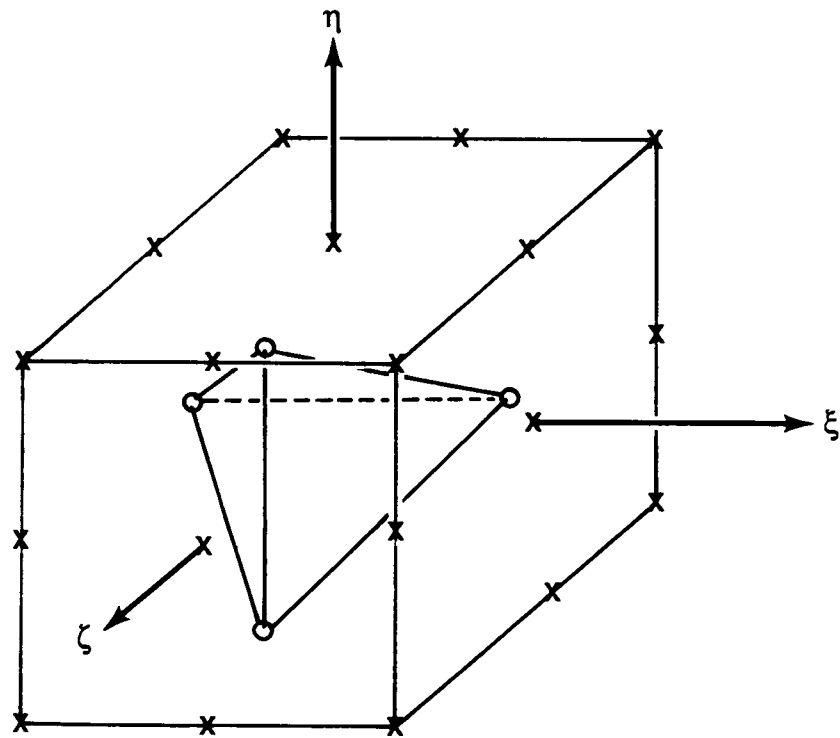
Label	ψ	Label	ψ	Label	ψ
A	-2.0×10^{-4}	F	1.0×10^{-4}	K	3.467×10^{-3}
B	-1.5×10^{-4}	G	5.0×10^{-4}	L	3.480×10^{-3}
C	-5.0×10^{-5}	H	1.0×10^{-3}	M	3.50×10^{-3}
D	-1.0×10^{-5}	I	2.0×10^{-3}		
E	0.	J	3.0×10^{-3}		

**TABLE 5. PRESSURE CONTOUR LABEL FOR
BACKWARD-FACING STEP FLOW**

Label	Reynolds Number (Re)		
	400.	500.	800.
A	-7.0	-25.5	-75.8
B	-6.0	-23.0	-75.0
C	-4.0	-18.0	-73.5
D	0.0	-8.0	-65.0
E	6.0	0.0	-45.0
F	12.0	10.0	-30.0
G	20.0	15.0	-22.0
H	28.0	20.0	-14.0
I	32.0	25.0	-8.0
J	33.5	27.0	0.0
K	34.5	28.5	3.0
L	35.5	29.5	7.0
M	36.0	29.8	10.0
N	36.5	30.0	11.5
O	36.8	----	12.0



(a)



(b)

Figure 1. Flow elements. (a) 2-D element, (b) 3-D element, x: velocity nodes, o: pressure nodes.

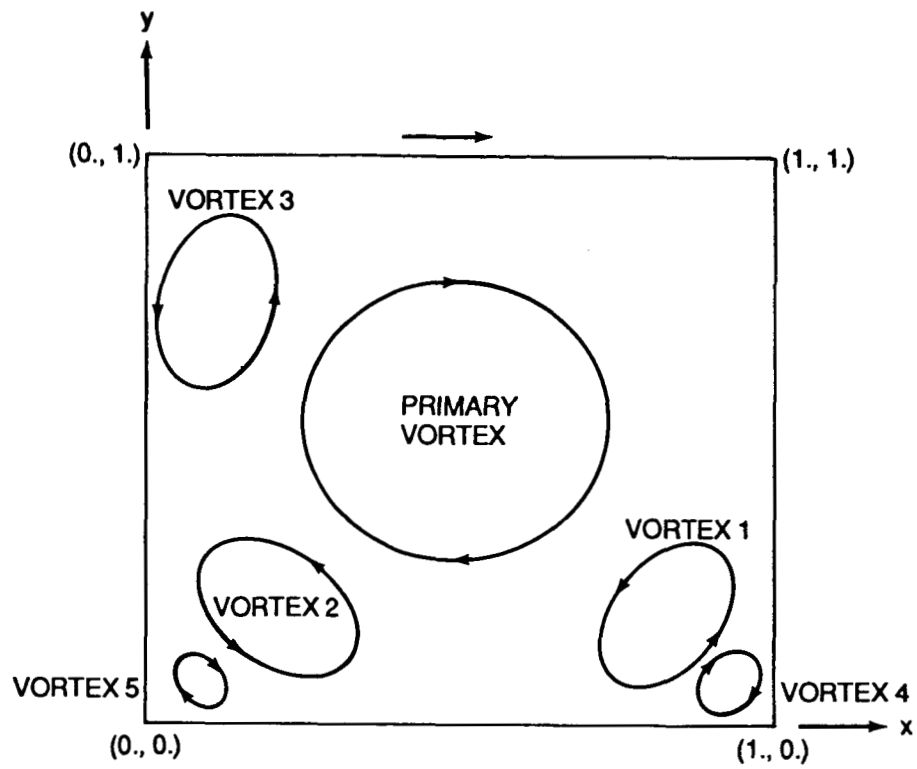
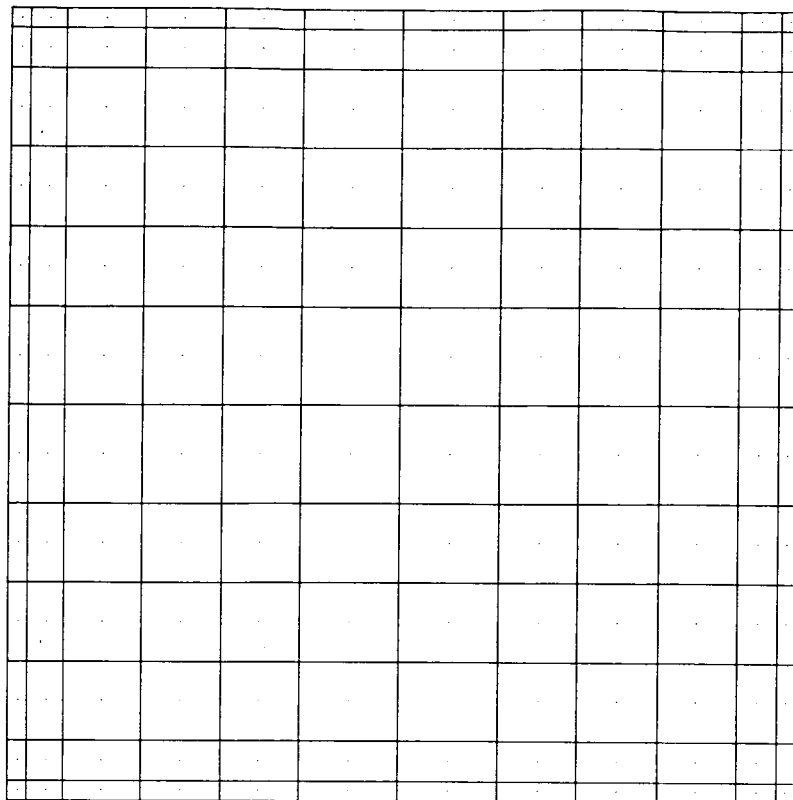
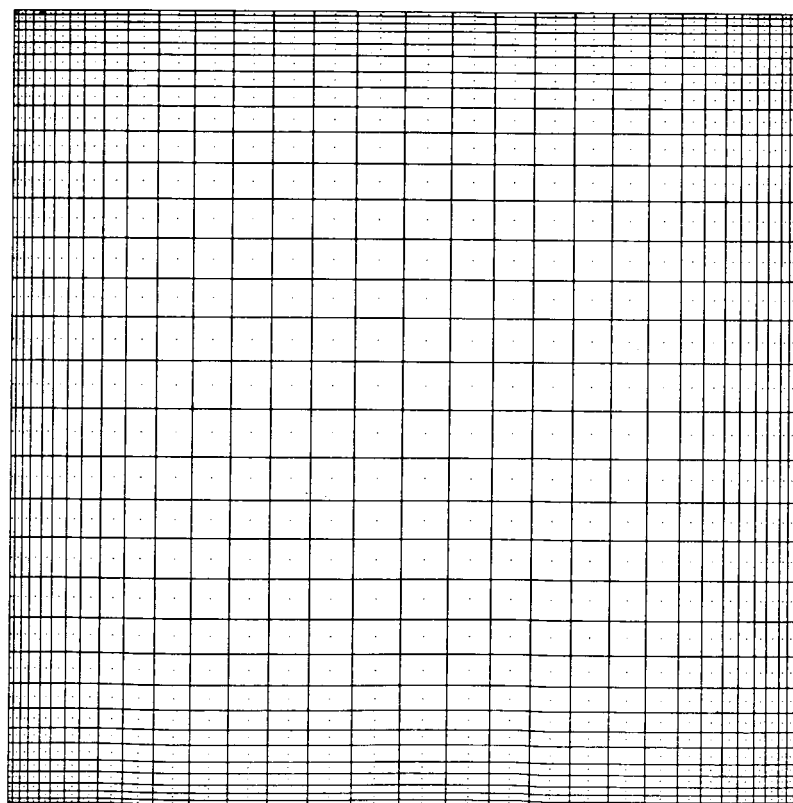


Figure 2. Configuration, coordinates, and nomenclature of cavity flow.

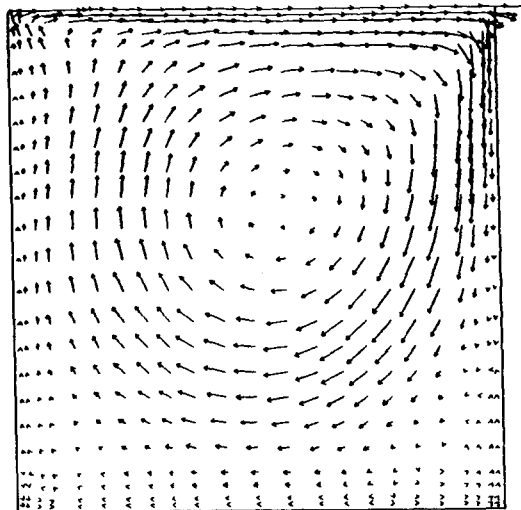


(a)

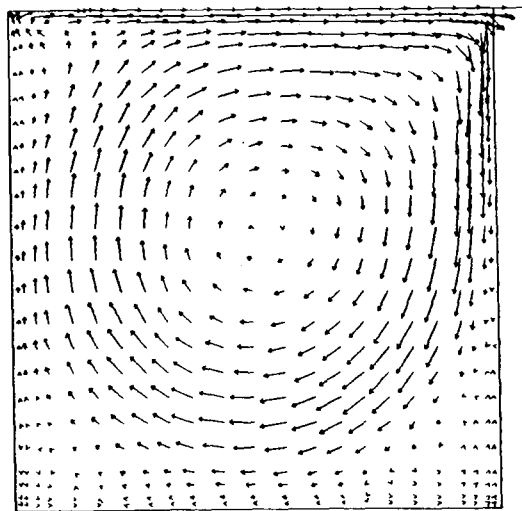


(b)

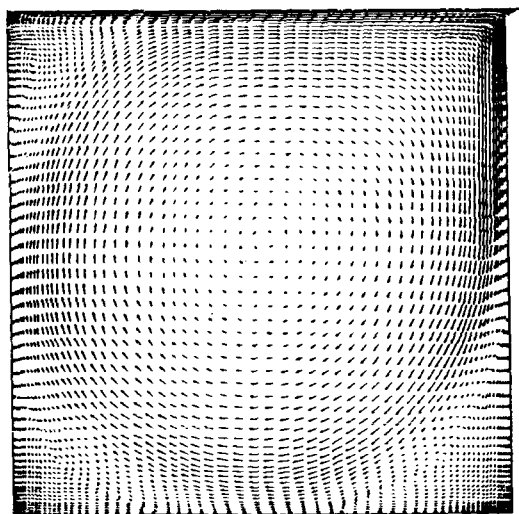
Figure 3. Discretization of cavity flow. (a) Grid A, 25x25 grids (12x12 quadratic elements). (b) Grid B, 65x65 grids (32x32 quadratic elements).



(a) $Re = 400$, GRID A

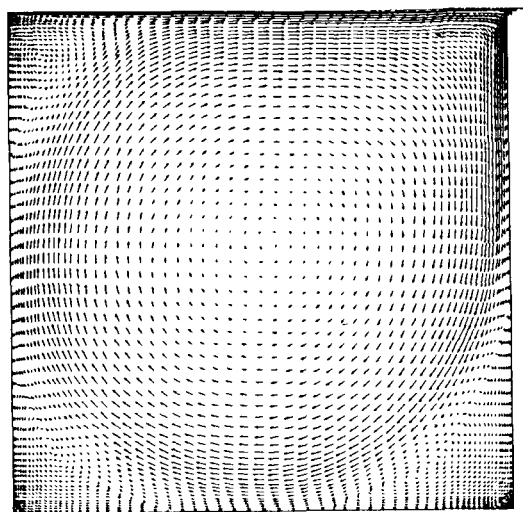


(b) $Re = 1,000$, GRID A

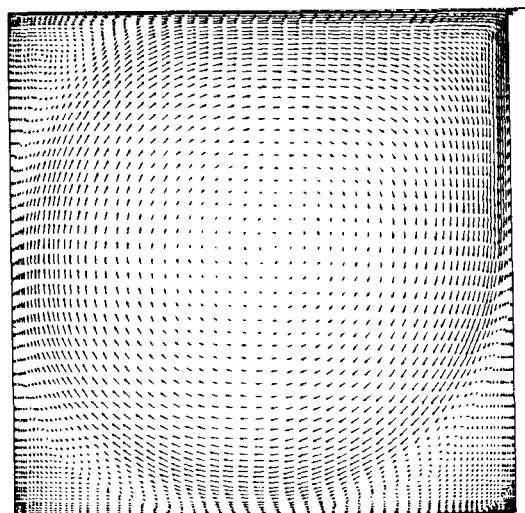


(c) $Re = 3,200$, GRID B

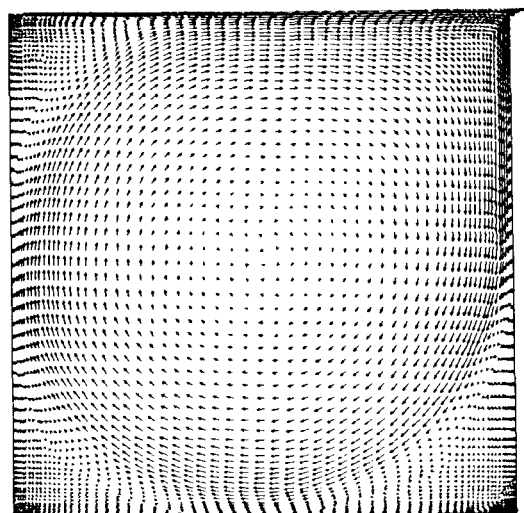
Figure 4. Velocity vectors for cavity flow, Re : Reynolds number.



(d) $Re = 5,000$, GRID B

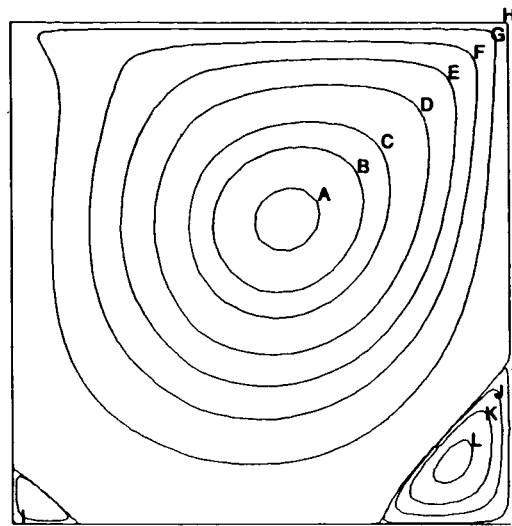


(e) $Re = 7,500$, GRID B

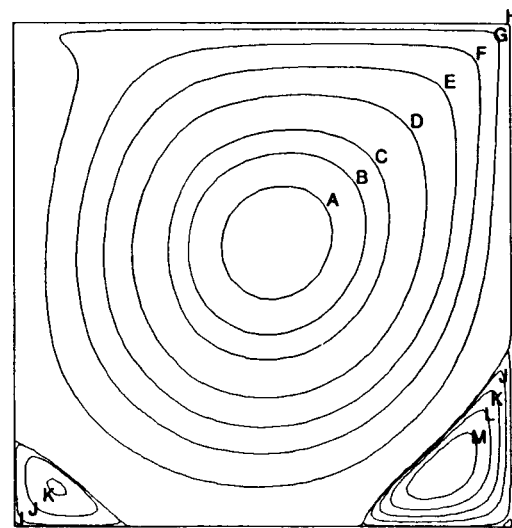


(f) $Re = 10,000$, GRID B

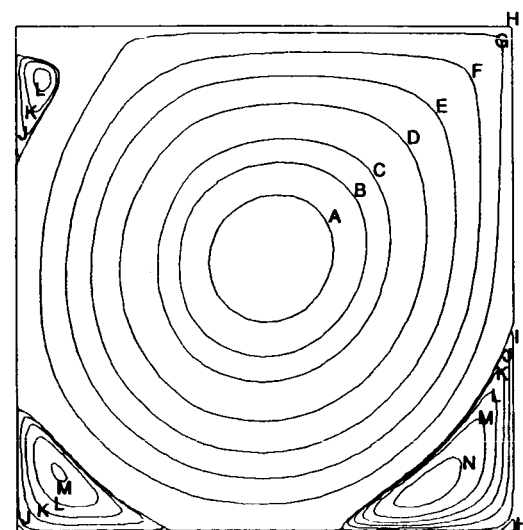
Figure 4. (Concluded)



(a) $Re = 400$

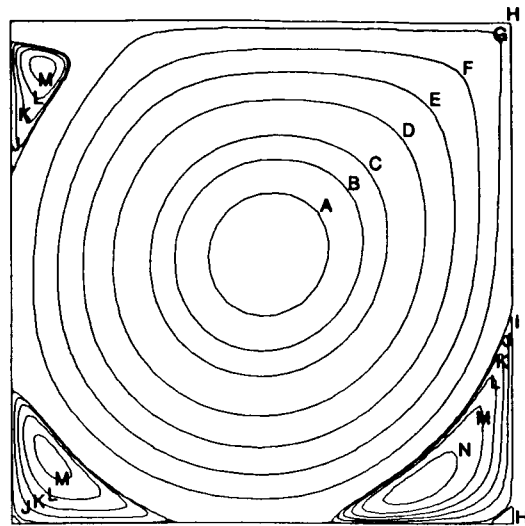


(b) $Re = 1,000$

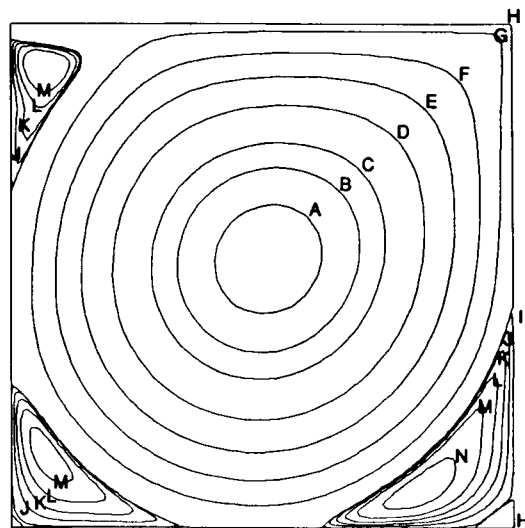


(c) $Re = 3,200$

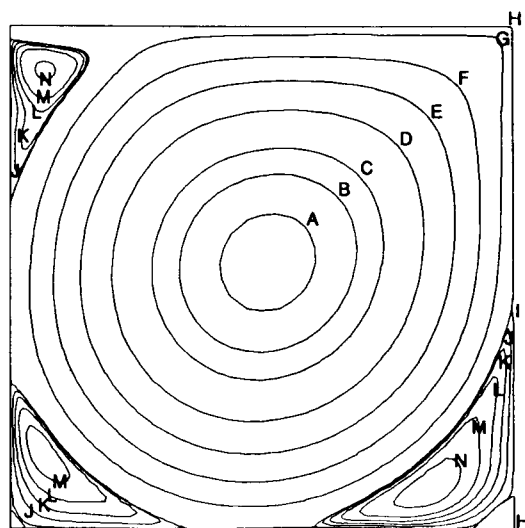
Figure 5. Streamlines for cavity flow.



(d) $Re = 5,000$

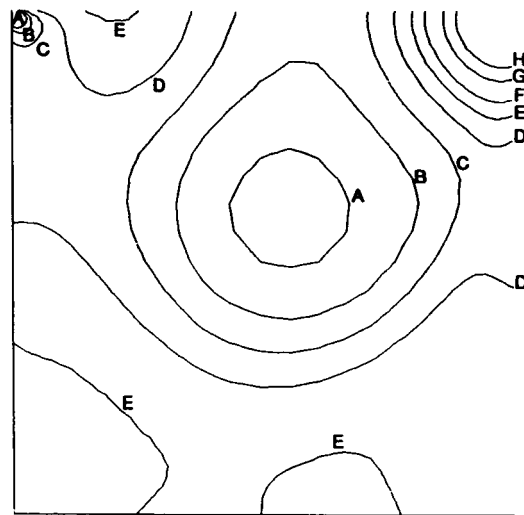


(e) $Re = 7,500$

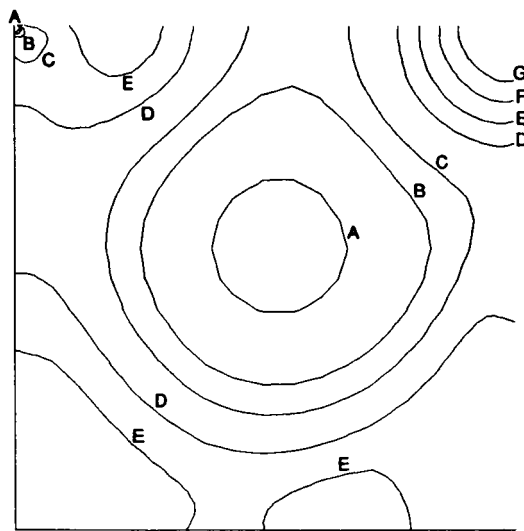


(f) $Re = 10,000$

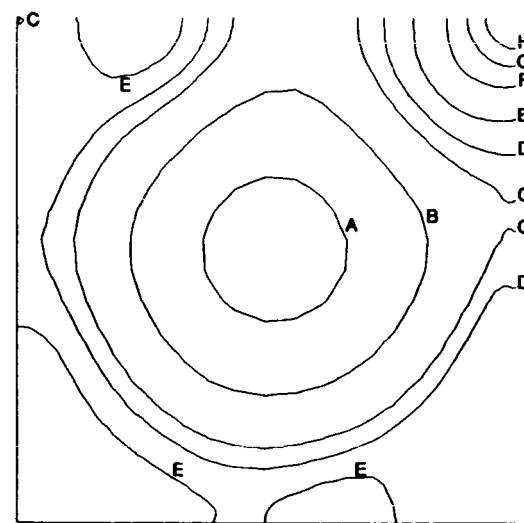
Figure 5. (Concluded)



(a) $Re = 400$

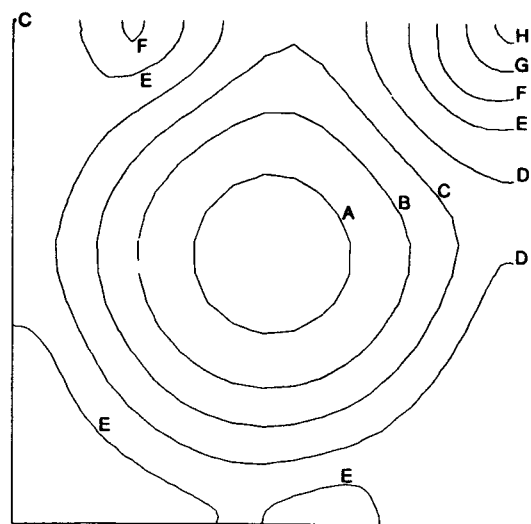


(b) $Re = 1,000$

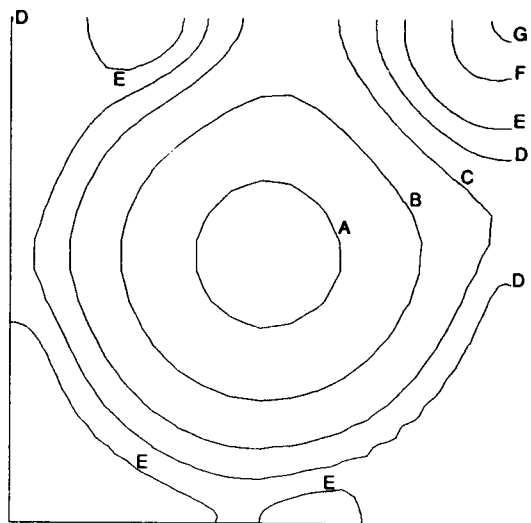


(c) $Re = 3,200$

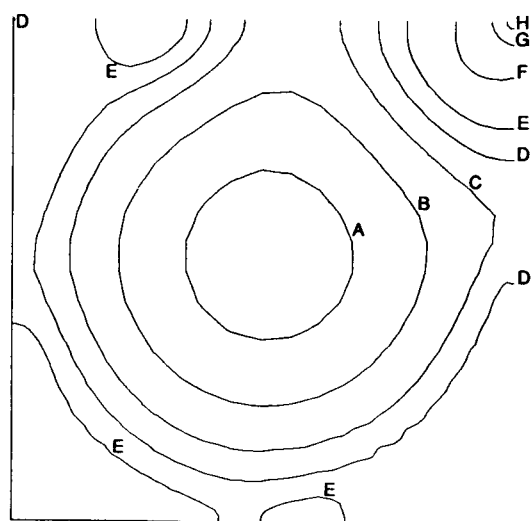
Figure 6. Pressure contours for cavity flow.



(d) $Re = 5,000$



(e) $Re = 7,500$



(f) $Re = 10,000$

Figure 6. (Concluded)

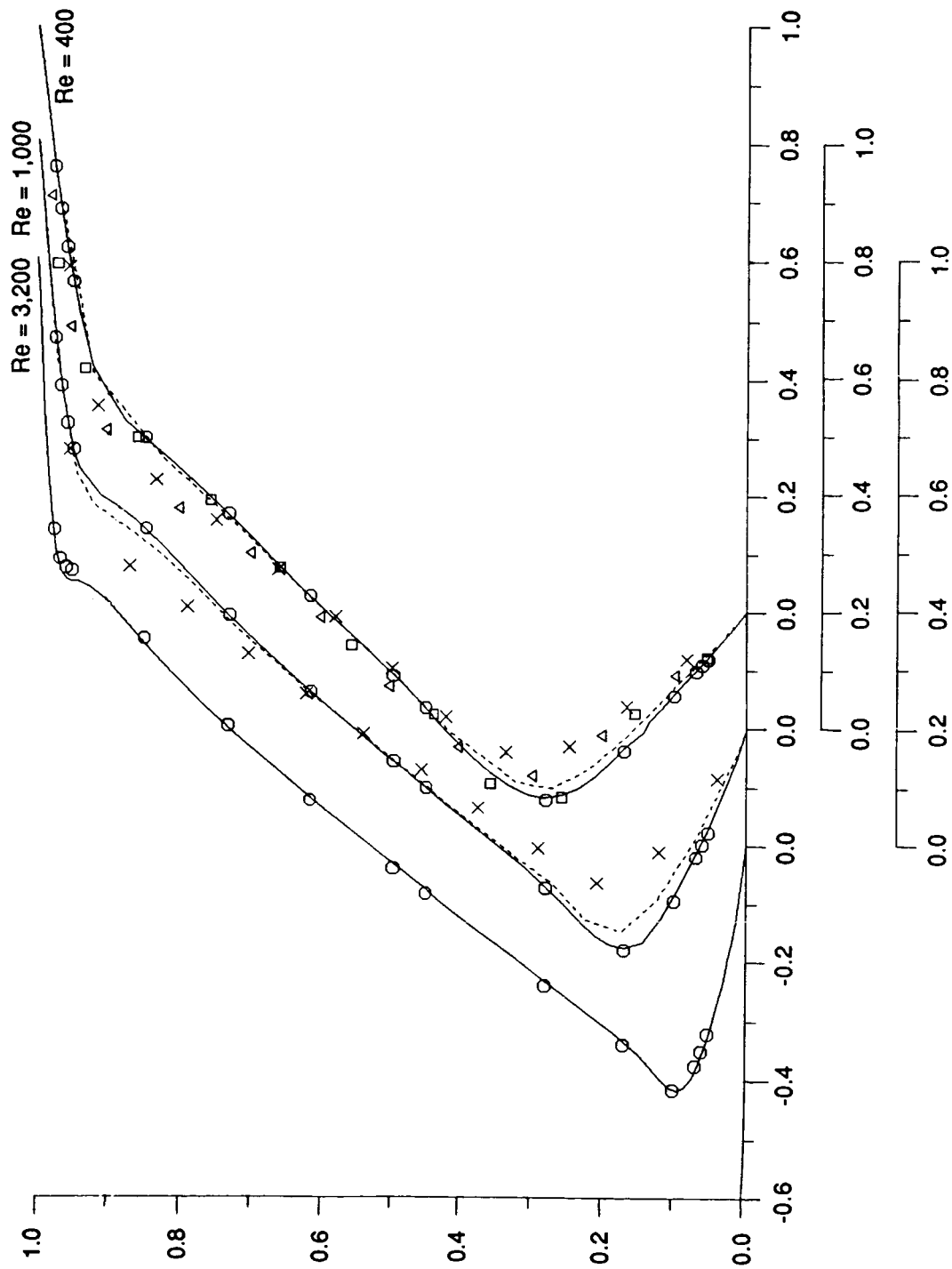


Figure 7. Horizontal velocity profiles of cavity flow at $x = 0.5$; - - -: present (Grid A),
 -----: present (Grid B), : Ghia et al. (129x129 grids), x: Bercovier and
 Engelman (25x25 grids), : Burggraf (41x41 grids), : Heinrich and
 Marshall (241x241 grids), : Schreiber and Keller (180x180 grids).

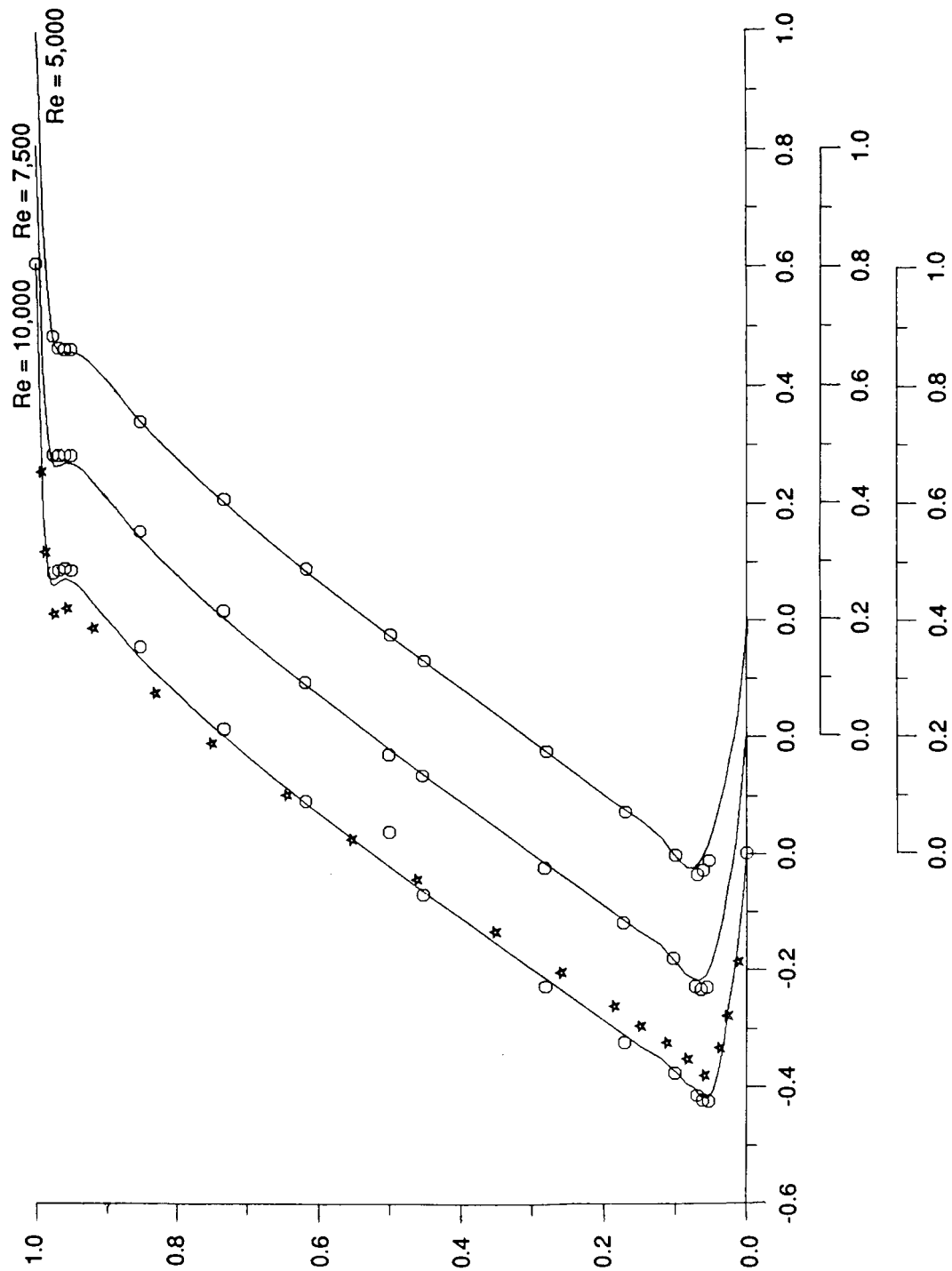


Figure 7. (Concluded)

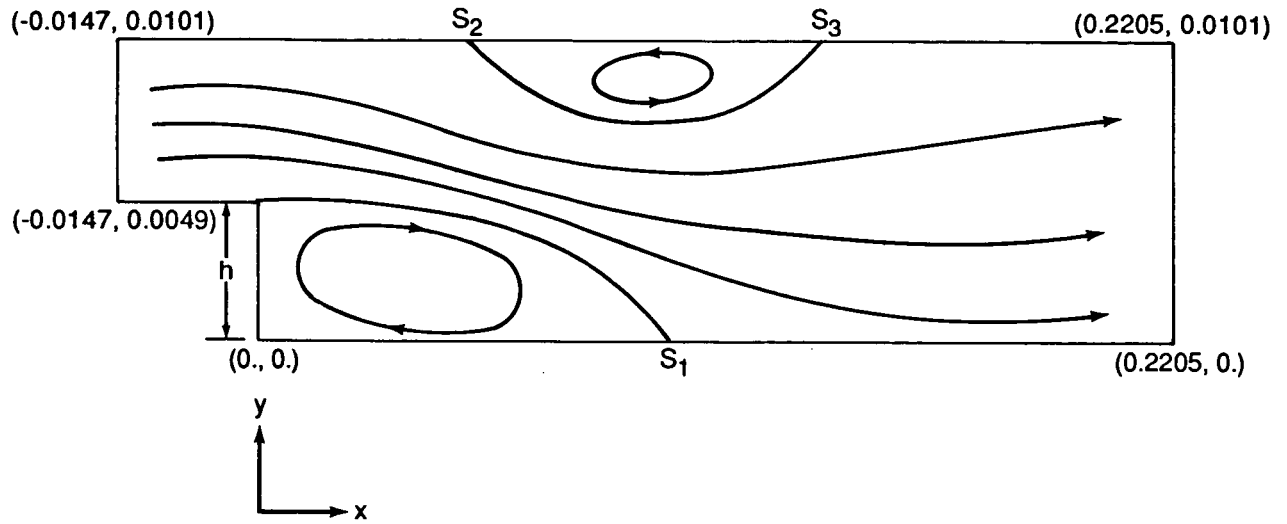
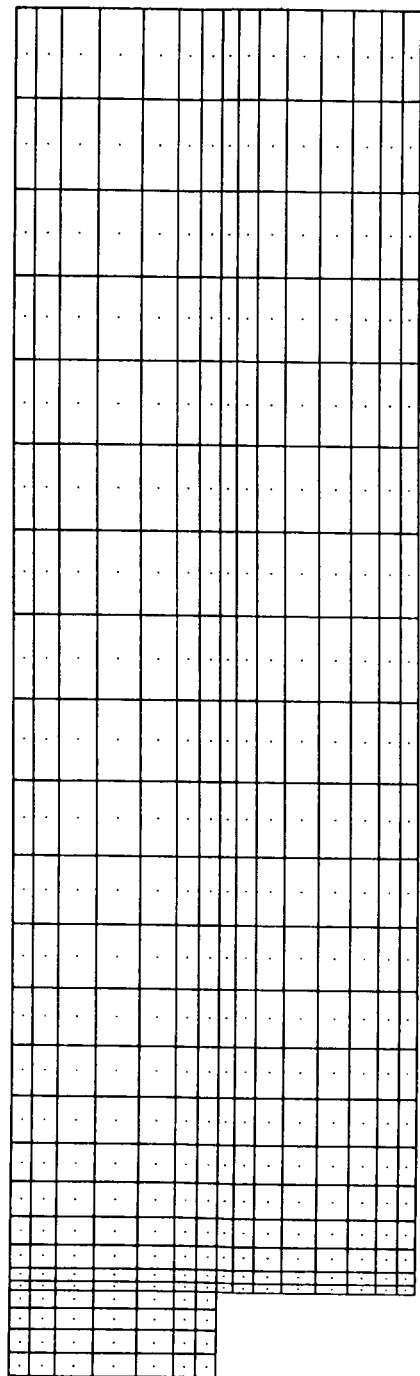
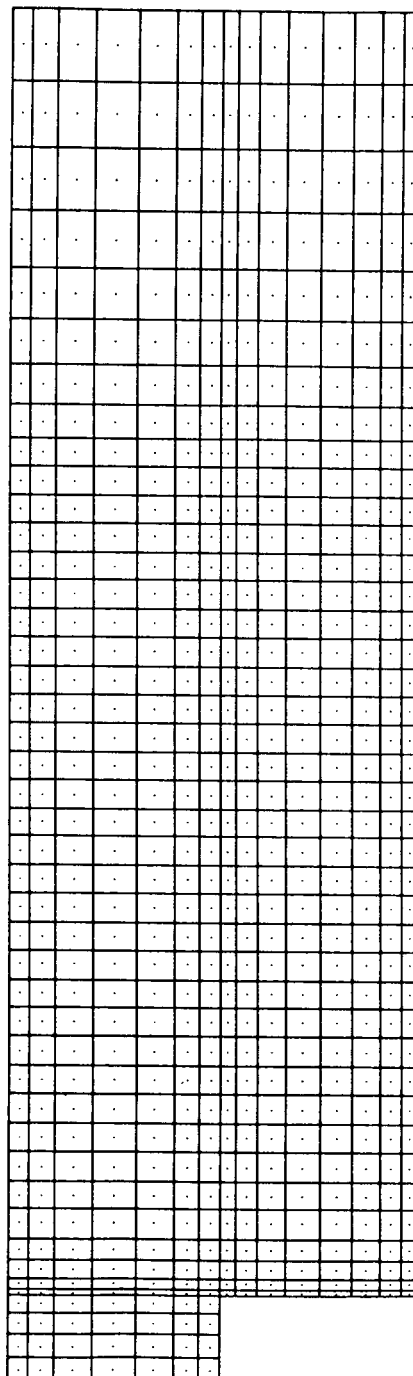


Figure 8. Configuration, coordinates and nomenclature of backward-facing step flow; h : step height (0.0049 cm).



(a)



(b)

Figure 9. Discretization of the backward-facing step flow; (a) Grid A, 51x31 grids (25x15 quadratic elements), (b) Grid B, 89x31 grids (44x15 quadratic elements).

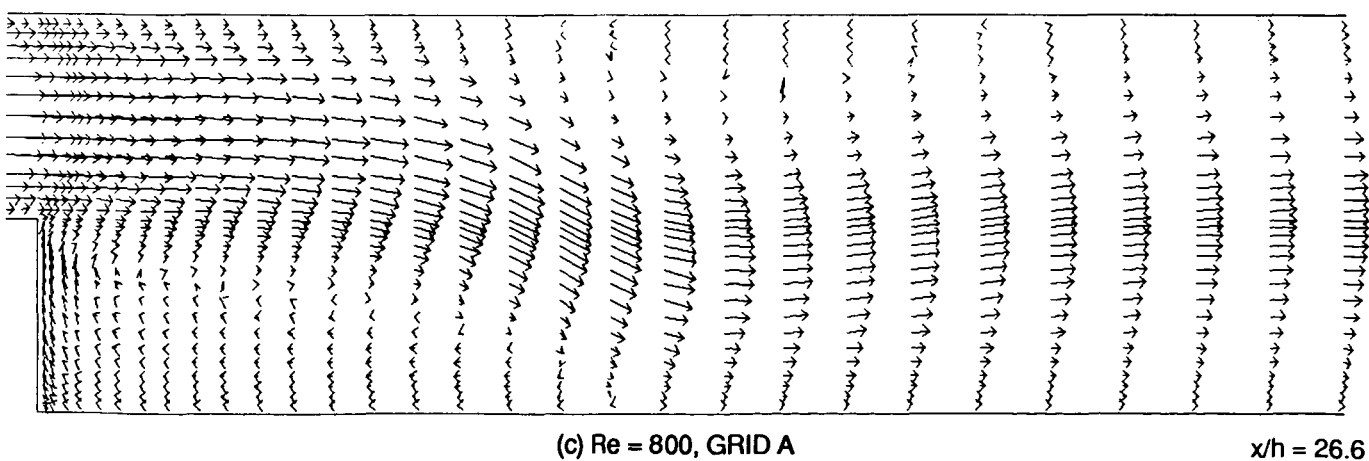
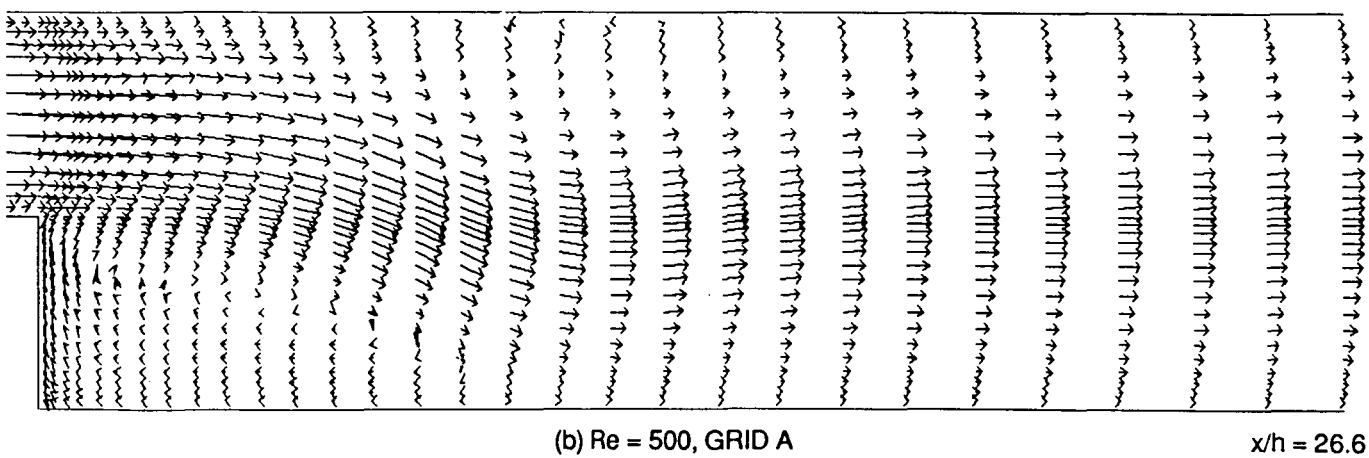
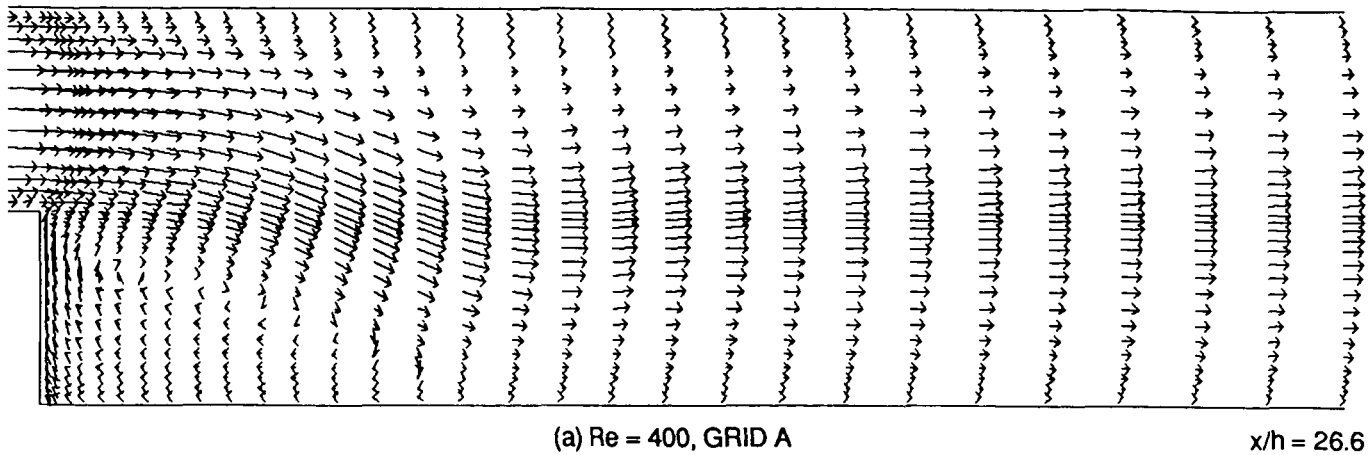


Figure 10. Velocity vectors for backward-facing step flow.

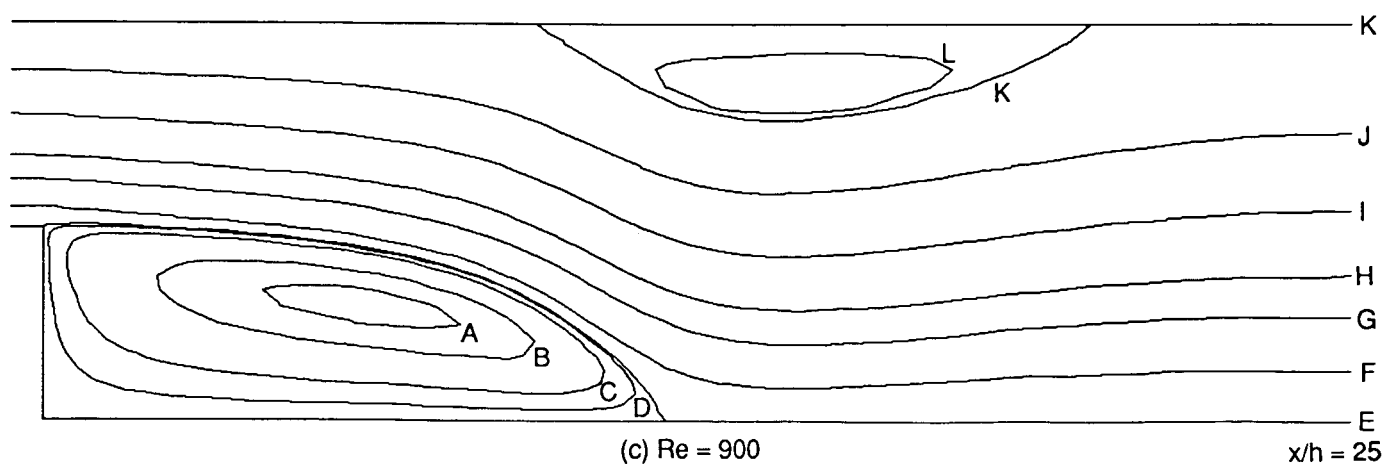
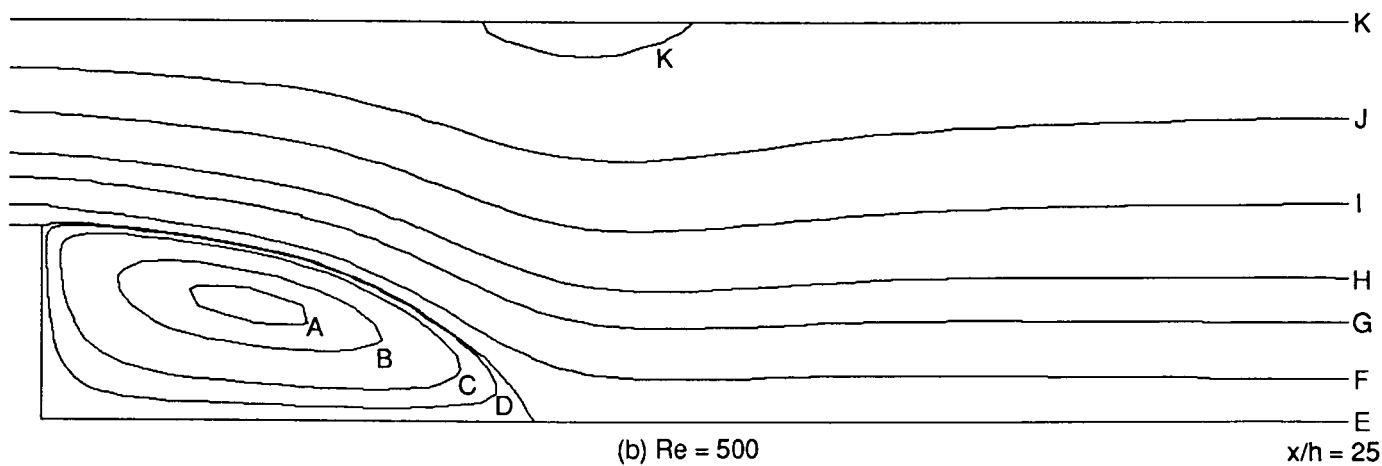
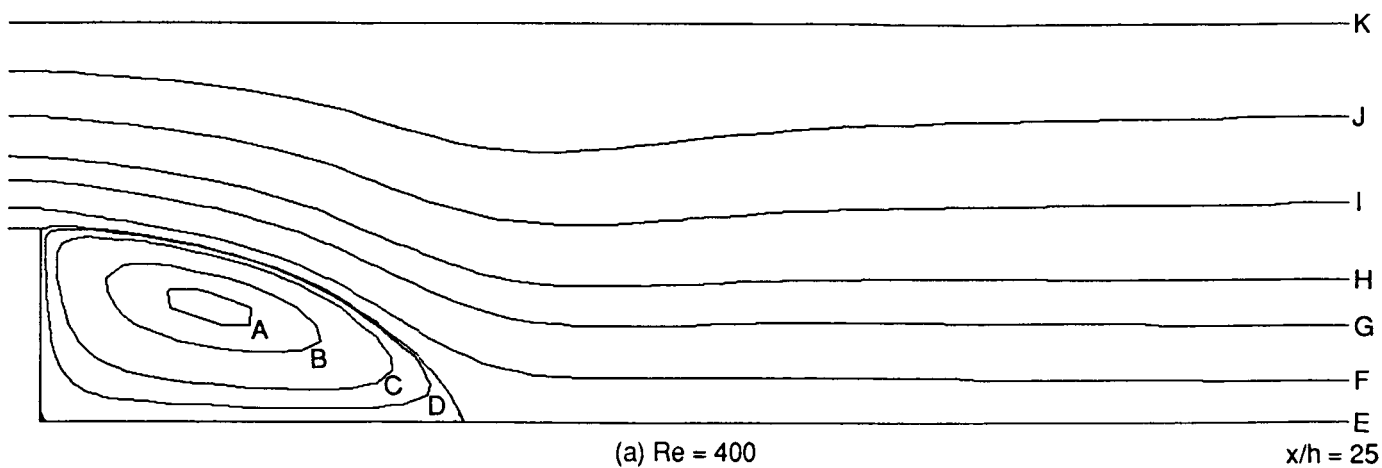


Figure 11. Streamlines for the backward-facing step flow.

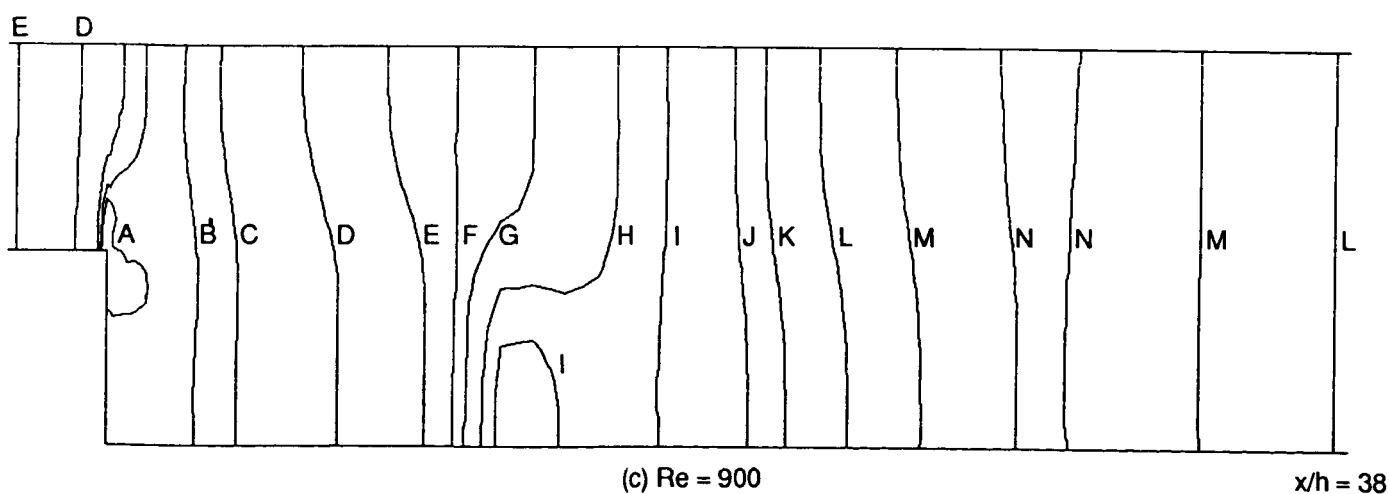
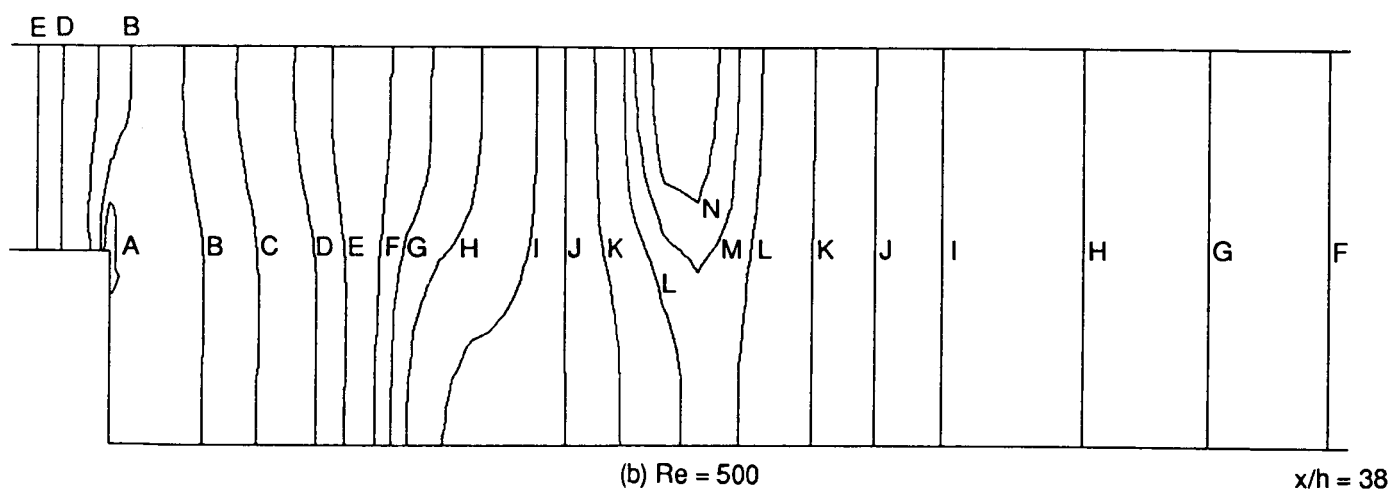
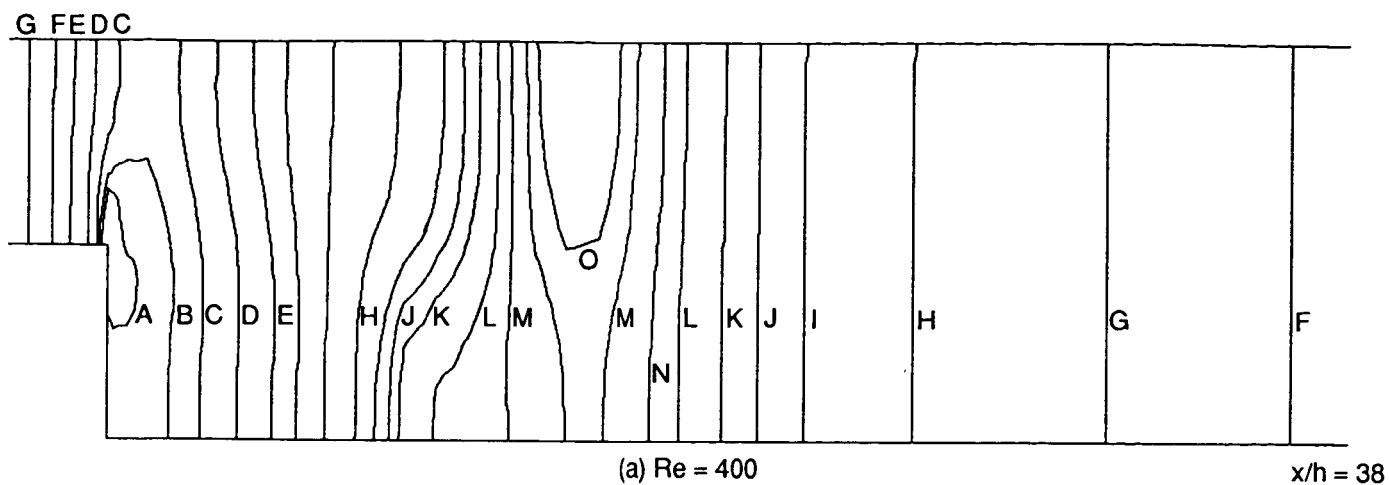


Figure 12. Pressure contours for the backward-facing step flow.

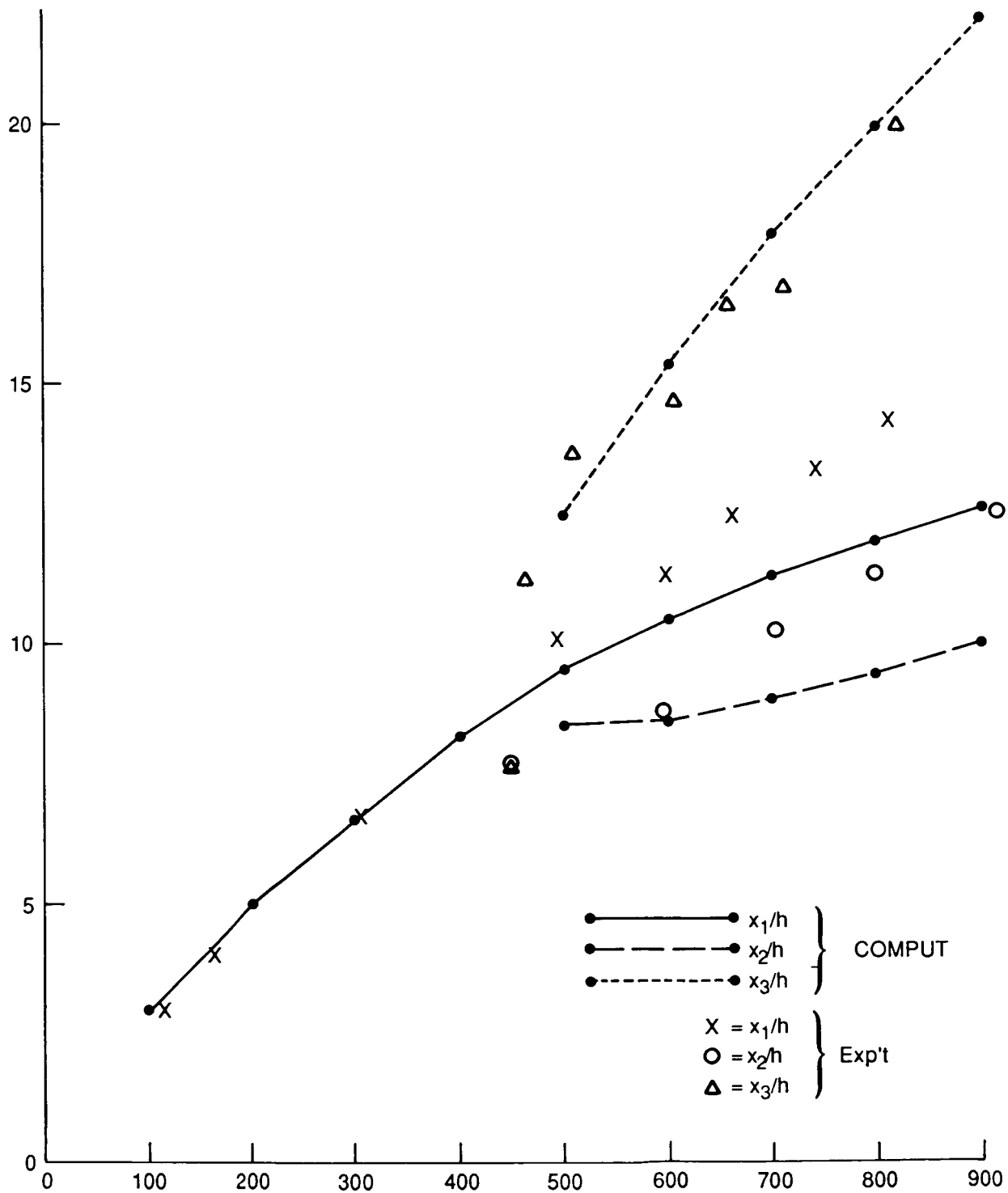


Figure 13. Reattachment length versus Reynolds number.

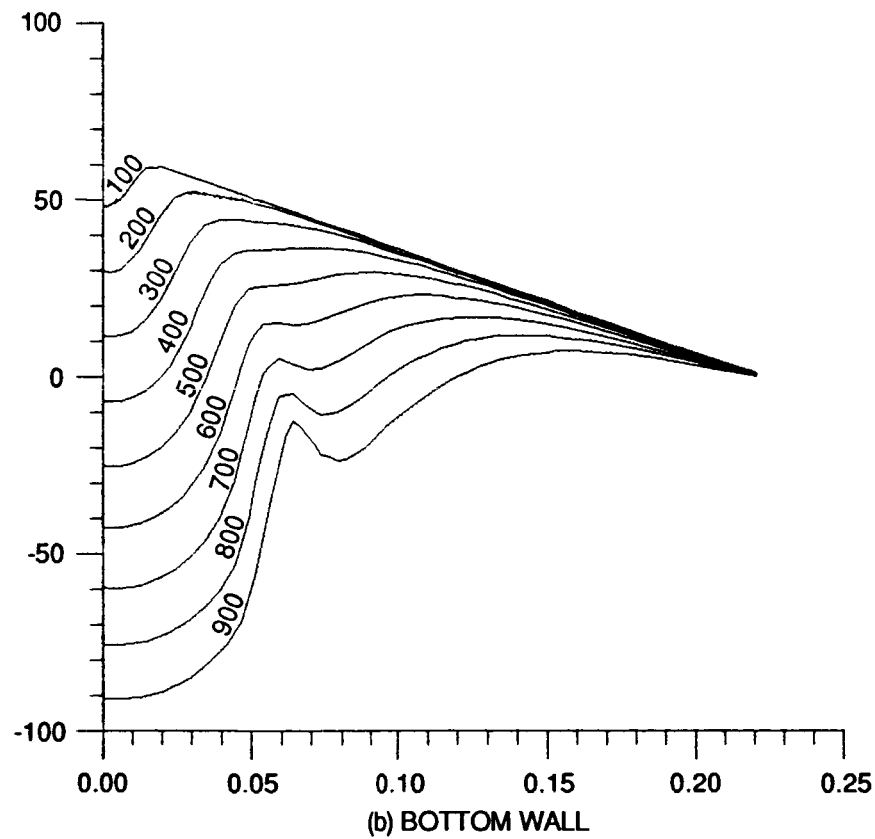
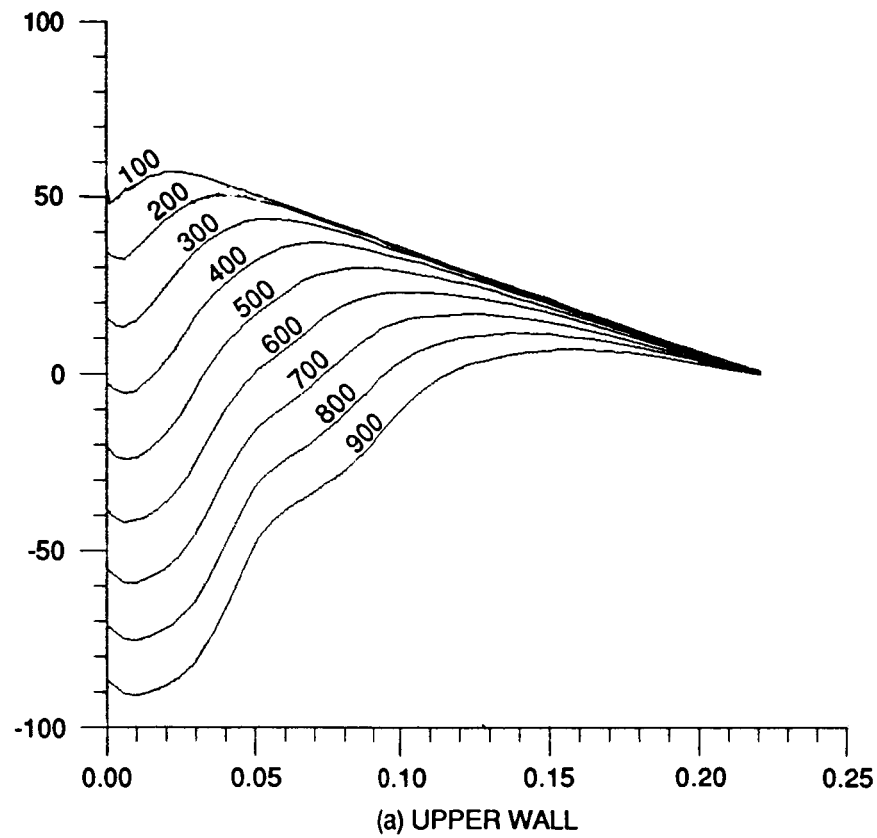


Figure 14. Wall pressure for backward-facing step flow, fine grid (Grid B) solutions, $Re = 100 - 900$.

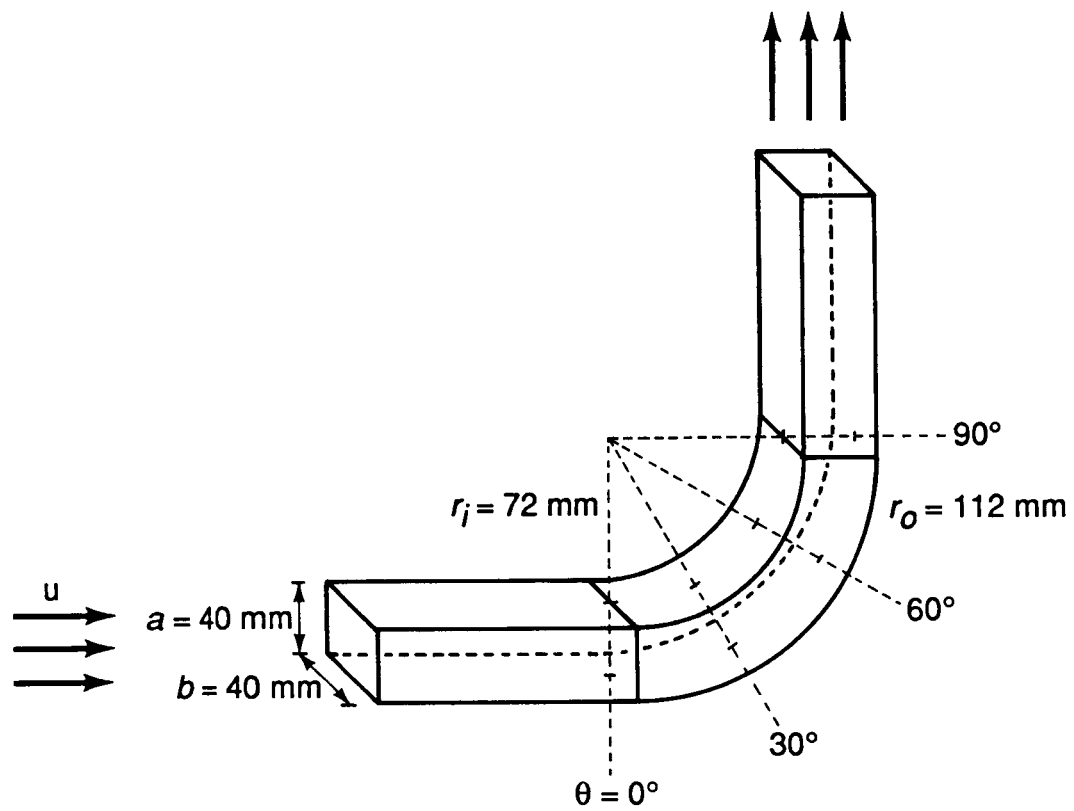


Figure 15. Configuration of the laminar flow in a square duct of strong curvature.

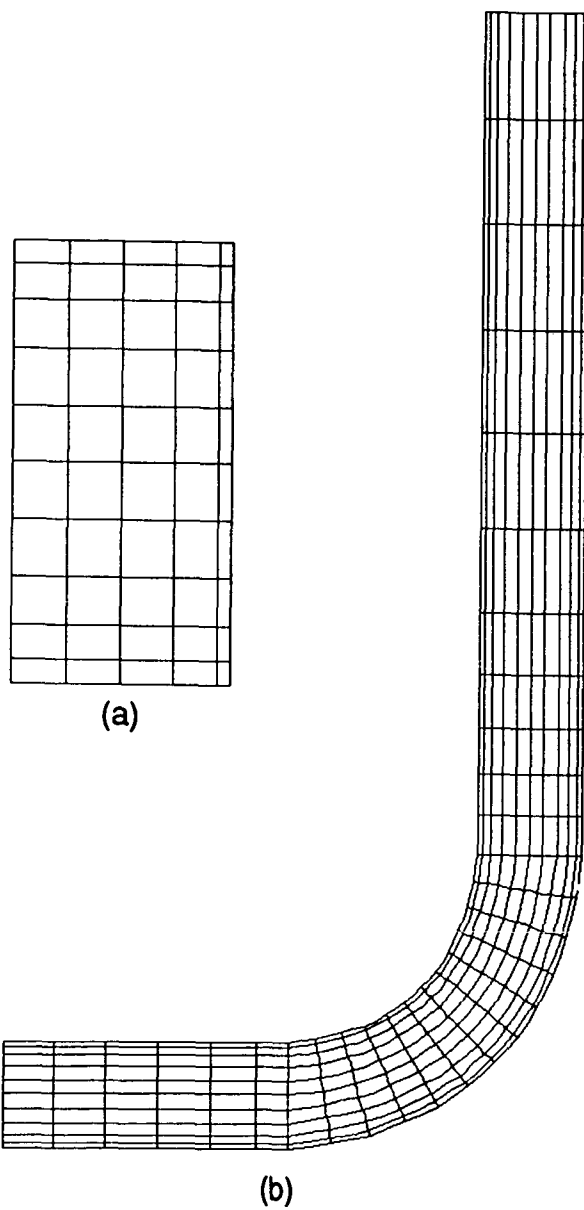


Figure 16. Discretization of the flow domain, (a) discretization of the cross-section, (b) grid in the flow direction.

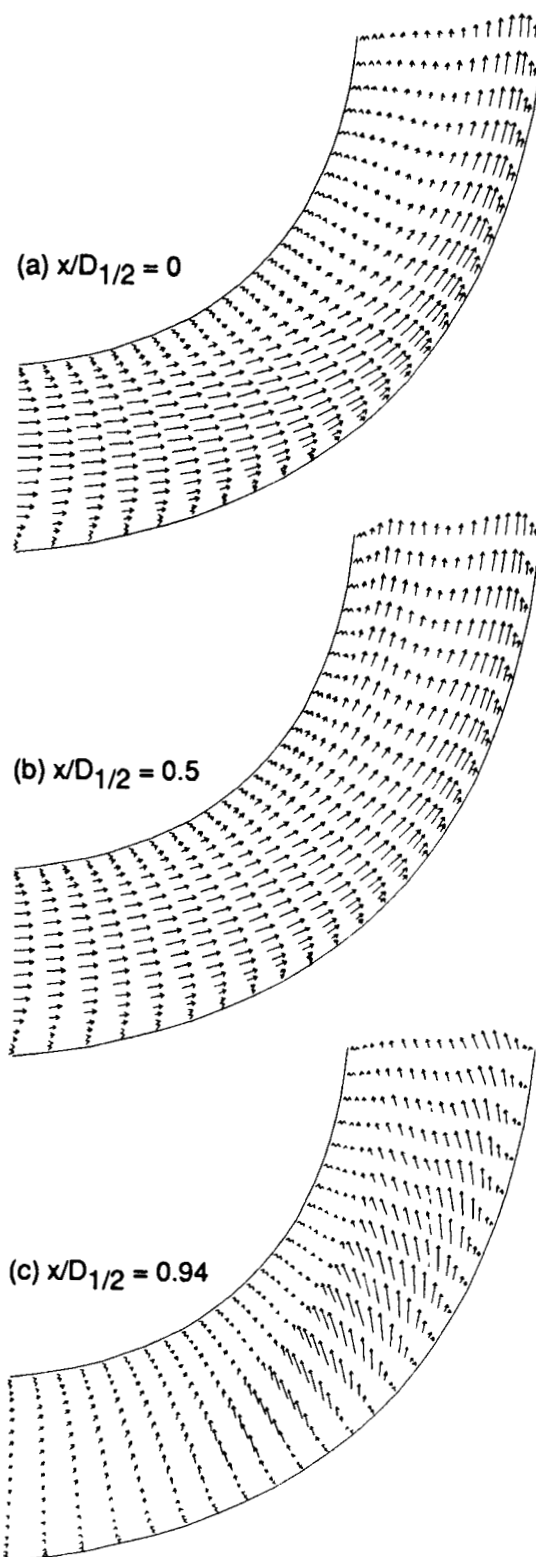
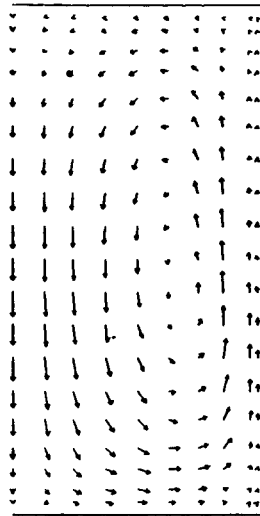
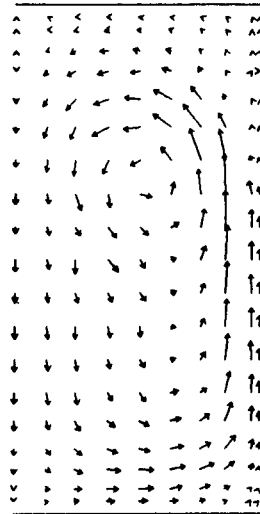


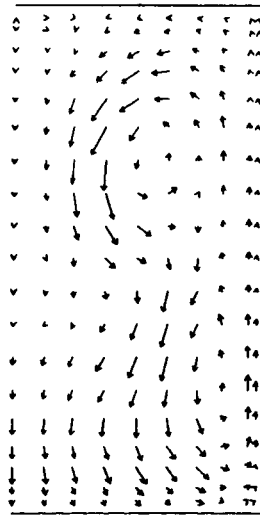
Figure 17. Velocity vectors on the curved section.
 (a) $x/D_{1/2} = 0$, (b) $x/D_{1/2} = 0.5$, (c) $x/D_{1/2} = 0.94$.



(a) $\theta = 30^\circ$



(b) $\theta = 60^\circ$



(c) $\theta = 90^\circ$

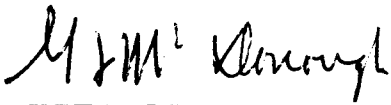
Figure 18. Secondary recirculation flows.
(a) $\theta = 30^\circ$, (b) $\theta = 60^\circ$, (c) $\theta = 90^\circ$.

APPROVAL

A FINITE ELEMENT COMPUTATIONAL METHOD FOR HIGH REYNOLDS NUMBER LAMINAR FLOWS

By Sang-Wook Kim

The information in this report has been reviewed for technical content. Review of any information concerning Department of Defense or nuclear energy activities or programs has been made by the MSFC Security Classification Officer. This report, in its entirety, has been determined to be unclassified.



G. F. McDONOUGH

Director, Systems Dynamics Laboratory